OPEN ACCESS

University of
BRISTOL

Peer reviewed version

Link to published version (if available):
10.1093/petrology/egu074

Link to publication record in Explore Bristol Research
PDF-document

Experimental Evidence for Polybaric Differentiation of Primitive Arc Basalt beneath St. Vincent, Lesser Antilles

Elena Melekhova[1*], Jon Blundy[1], Richard Robertson[2], Madeleine C.S. Humphreys[3]

[1]School of Earth Sciences, University of Bristol, Wills Memorial Building, Bristol BS8 1RJ, UK

[2]Seismic Research Centre, University of the West Indies, St. Augustine, Trinidad & Tobago, West Indies

[3] Department of Earth Sciences, Durham University, Science Labs, Durham DH1 3LE, UK

[*]Corresponding author. Telephone: +44 (0) 117 331 5181; Fax: +44 (0) 117 925 3385; E-mail: lena.melekhova@bristol.ac.uk.

ABSTRACT

Equilibrium crystallisation experiments have been performed on a primitive high-MgO basalt (HMB) from Soufrière, St Vincent, with three different initial H_2O contents (0.6, 2.3 and 4.5 wt%), at pressures of 0.4, 0.7, 1.0 and 1.3 GPa and temperatures from 1350 to 950 °C. Redox conditions, as determined by μXANES analysis of Fe^{3+} in experimental glasses, lay 1 to 4 log units above the NNO buffer. The aim of the study was to explore the differentiation conditions that gave rise to the observed geochemical variation in lavas and plutonic (cumulate) xenoliths from St. Vincent. An experiment with 4.5 wt% initial H_2O is multiply-saturated close to its liquidus (1180 ºC and 1.3 GPa) with a spinel lherzolite assemblage, which is consistent with a primary origin for HMB in the mantle wedge. Multiple saturation of HMB with 2.3 wt% H_2O was not observed, but is inferred to occur at pressures >1.3 GPa.

The experimental results show that initial H_2O content has significant influence on differentiation paths of primary HMB magma, with different lava varieties generated under discrete, well-constrained P-T-H_2O conditions. Low-magnesian basalts (LMB) can be generated from HMB with 2.3-4.5 wt% H_2O at pressures of 1.0 to 1.3 GPa, corresponding to Moho depths beneath St. Vincent. The CaO contents of LMB are sensitive to differentiation pressure: high CaO LMB are produced at pressures > 0.5 GPa. Basaltic andesites (BA) can be generated at 0.7-1.0 GPa from HMB with 0.6-2.3 wt% H_2O. High-alumina basalts (HAB) are produced at mid-upper crustal conditions ($\leq$ 0.4 GPa) by differentiation of HMB with high initial H_2O ($\geq$4 wt%) through delay of plagioclase crystallisation and dominant fractionation of olivine, clinopyroxene and spinel. St Vincent andesites could be produced from relatively dry ($\leq$ 0.6 wt% H_2O) HMB only at lower crustal conditions. This is suggestive of a partial melting origin from precursor HMB that had solidified at depth to produce gabbros with ~30% hornblende, i.e. ~0.6 wt% structurally-bound H_2O. The experimentally-determined differentiation conditions are consistent with polybaric differentiation within a hot zone that extends from the Moho and uppermost mantle to the mid or upper crust. Within the hot zone differentiation occurs by a combination of crystallisation of HMB with 2-5 wt% H_2O and partial melting of ancestral HMB gabbros. Although, the experimental melts provide an excellent match to erupted lava compositions, experimental crystal compositions do not match either phenocrysts or cumulate crystals, as preserved in xenoliths. The failure to reproduce natural crystal compositions suggests that these are formed as differentiated magmas ascend and attain their H_2O-saturated liquidi at shallower pressures. Thus there is a disconnect between the high-pressure phase compositions and assemblages that generate liquid compositional diversity and the low-pressure composition and assemblages that occur as phenocrysts and in cumulate xenoliths. This finding lends support to the idea of cryptic fractionation in the generation of arc magmas.

INTRODUCTION

The primary mechanism of magma generation above subduction zones involves partial melting of peridotite mantle wedge by the addition of H_2O-rich, slab-derived fluids. The resultant primitive magmas are MgO-rich basalts (or picrites) with ≤ 5 wt% dissolved H_2O. Such MgO-rich magmas are known from volcanic arcs. However, they are relatively rare, with examples limited to intra-oceanic arc systems such as Izu-Bonin-Marianas, Lesser Antilles, Solomon Islands, Vanuatu, New Britain, South Sandwich and Kamchatka (e.g. Yamamoto 1988; Eggins, 1993; Macdonald et al., 2000; Schuth et al., 2004; Portnyagin et al., 2007). At the vast majority of arcs the dominant erupted magma type is too evolved to have equilibrated directly with mantle peridotite testifying to the importance of subsequent differentiation of primitive magmas in generating more evolved compositions (e.g. Brophy, 1989; Ozerov, 2000; Toothill et al., 2007). Differentiation may occur either in the uppermost mantle wedge or within the overlying crust, and involve fractional crystallization with or without crustal assimilation (partial melting).

Here we evaluate the chemical consequences of basalt differentiation in the mid to lower crust and uppermost mantle (0.4 to 1.3 GPa pressure) by means of experiments on a primitive basalt from St. Vincent (Lesser Antilles) with initial H_2O contents of 0.6, 2.3 and 4.5 wt%. Limited data from the same suite of experiments reported were presented in Melekhova et al (2013); here we present the experimental results in greater detail, including phase compositions, and place the results in the wider context of magma generation beneath St. Vincent. Our goal is to constrain the conditions under which primitive basalt differentiation can generate the observed chemical diversity of erupted magmas on St. Vincent as well as the compositions of minerals in cumulate xenoliths from the island.

Volcanic Geology of St. Vincent

St Vincent lies at the southern end of the Lesser Antilles, a 750 km-long intra-oceanic arc (Fig. 1a, b). The abundant, closely-spaced volcanic centres, small age range of the subducted plate (e.g., Macdonald & Holcombe, 1978), wide range in geochemistry of volcanic rocks (Brown et al., 1977, Macdonald et al., 2000; Pichavant & Macdonald, 2007), unusually high incidence of plutonic xenoliths (Lewis, 1973 a, b; Arculus & Wills, 1980) and occurrence of high-MgO basalts, make the Lesser Antilles a unique natural laboratory for understanding magma differentiation processes. St. Vincent is one of only two islands in the arc (the other being Grenada) that have erupted primitive MgO-rich basalt (MgO ~ 14.5 wt%; Heath et al., 1998a; Robertson, 2002). The plutonic xenoliths, include gabbros, troctolites and rare hornblende-clinopyroxenites (Arculus & Wills, 1980; Tollan et al., 2012).

St. Vincent is entirely volcanic with lava flows and pyroclastic deposits ranging in composition from basalts through basaltic andesites to rare andesites. Basalt dominates the southernmost parts of the island, whereas basaltic andesites dominate further north. Basalts and basaltic andesites are most common during the early evolutionary stages of individual volcanic centres, whereas andesites characterise the waning stages of activity most commonly forming dykes and late-stage domes or central plugs. Radiometric dating indicates a northward migration from 3 Ma near the south of the island, to 0.6 Ma at the Soufrière volcano (Rowley, 1978b; Briden *et al.*, 1979; Heath *et al.*, 1998a). However, the northward migration is not systematic and activity within and between individual centres may have overlapped.

The island is divided into four major geologic regions (Fig. 1b). The Soufrière Volcanic Centre, the youngest on St. Vincent (last eruption 1979), occupies the northernmost third of the island and rises to 1178 m (Rowley, 1978b; Robertson, 1992). The oldest formations (~690 ka), exposed on the flanks, are basaltic lavas, which form the remnants of the pre-historic Somma crater.

Petrology of Lavas

St. Vincent lavas, from basalt to andesite, contain phenocrysts of olivine, plagioclase, Fe-Ti oxides, clinopyroxene and orthopyroxene. Amphibole is conspicuously absent. The basalts are divided in to three varieties: high magnesium (HMBs, MgO > 10 wt%), low magnesium (LMBs, MgO > 6wt % wt%) and high alumina (HABs, MgO $\leq$ 6 wt%, $Al_2O_3 \geq$ 19 wt%). This distinction is used throughout this paper.

HMBs consist mainly of olivine (Fo_{75-89}) phenocrysts and microphenocrysts and rare microphenocrysts of clinopyroxene (Wo_{38-45}). Cr-spinel is the sole oxide, occurring as inclusions in olivine and rarely as fine-grained euhedral to subhedral phenocrysts.

LMBs are porphyritic (5-44 vol.% phenocrysts, 0-19 vol.% microphenocrysts) with a distinct variation in grain-size, texture and phenocryst assemblages related to MgO content. LMBs with MgO > 6wt % are texturally similar to HMBs, with olivine- or pyroxene microphenocrysts; plagioclase phenocrysts are scarce or absent. There are two types of olivine in LMBs: small to medium grained, lath-shaped, strongly zoned crystals with an average composition of Fo_{50-70} and, possibly xenocrystic, large, often corroded crystals with cores of Fo_{67-90}. There are two oxide varieties: Ti-magnetite and Cr-spinel. Clinopyroxenes are normally zoned and divided into large phenocrysts (Wo_{36-43}) and small- to medium-sized phenocrysts (Wo_{23-43}). Diopside (Wo_{45-50}) occurs mainly as cores of augite crystals and rarely as discrete phenocrysts. Orthopyroxene (En_{47-70}) occurs as normally zoned phenocrysts. There is a wide range in plagioclase compositions – average rims are An_{17-74} and cores An_{57-90}. Crystals are mainly normally zoned, although some crystals with reverse zoning occur.

HABs overlap completely with LMBs in terms of all major elements except for Mg and Al. They contain olivine- or pyroxene microphenocrysts and plagioclase phenocrysts. Although HABs are generally richer in modal plagioclase phenocrysts than LMBs,

correlations between Al_2O_3 and CaO do not extrapolate to the composition of plagioclase cores in these rocks (typically An_{65-90}), suggesting that their Al-rich character is not a result of plagioclase accumulation, but a primary chemical feature.

The phenocryst assemblage of basaltic-andesites is similar to that of LMB, from which they can be distinguished by a greater abundance (15-53 vol%) of phenocrysts of clinopyroxene, represented by diopside (Wo_{48}) and augite (Wo_{41}), orthopyroxene (En_{56-67}) and plagioclase (An_{49-95}). Olivine phenocrysts (cores Fo_{53-86}, rims Fo_{56-66}) are scarce. Titanomagnetite is the only oxide phase.

Rare St. Vincent andesites are porphyritic (11-35 vol.% phenocrysts, 5-13 vol.% microphenocrysts) with greater quantities of pyroxenes than basalts and basaltic-andesites. Olivine (Fo_{82-84}) is rare. Clinopyroxene is represented by sub-equal proportions of augite (Wo_{36-44}) and diopside (Wo_{45-49}). Some clinopyroxene grains are zoned whereas others have a reaction rim. Occasionally there are complete plagioclase pseudomorphs after pyroxene. Orthopyroxene (En_{55-70}) is normally zoned. Plagoclase phenocrysts are heterogeneous with a wide range in core composition (An_{54-94}). Titanomagnetite is the sole oxide phase.

Plutonic Xenoliths

St Vincent plutonic xenoliths are predominantly composed of olivine – plagioclase – clinopyroxene – hornblende and oxides (Arculus & Wills, 1980; Tollan et al, 2012). In contrast to phenocrysts in lavas, amphibole is an abundant cumulus phase, whereas orthopyroxene is universally lacking. Truly ultramafic xenoliths are rare; of 50 samples of cumulate xenoliths collected from St. Vincent only one is a hornblende-pyroxenite. Olivine-gabbros are the most common xenolith type with hornblende as an additional phase, often in significant amounts. Troctolites are the second most common type, characterized by the predominance of olivine over clinopyroxene. Plagioclase hornblendites are the third most

common cumulate type, characterised by high modal plagioclase in some samples (Tollan et al 2012).

Olivine occurs in all xenolith samples but one (hornblende-pyroxenite, VS20) with modal abundances reaching 60 vol% (Tollan et al 2012). Olivine does not display any significant zoning (Lewis, 1973a, 1973b; Arculus & Wills, 1980; Tollan et al 2012). Plagioclase is the most abundant xenolith phase (up to 70 vol%). The striking feature of St Vincent xenoliths is the coexistence of relatively evolved olivine (Fo_{71-79}) with very calcic plagioclase (An_{95-85}). Clinopyroxene, where present, has a modal range up to 50 vol%, and is calcic augite with Mg# in the range 81-75. Clinopyroxenes display more chemical heterogeneity than any other phase, showing normal and reverse zoning (Tollan et al 2012, Arculus & Wills, 1980). Amphibole is magnesiohastingsite with Mg# $_{89-70}$ and a wide range of modal abundances (0-44 vol%, Tollan et al, 2012). Individual crystals may show normal or, rarely, reverse zoning. Amphiboles lack opacite breakdown rims, suggestive of fast ascent. The dominant spinel composition is high-Al, high-Mg titanomagnetite with Cr# 0.5- 2.5. In a single xenolith Tollan et al (2012) report pleonaste.

Isotope Geochemistry

Radiogenic isotope data (Sr, Pb, Nd) for St. Vincent magmas are presented by Heath et al. (1998a). There is little variation in $^{87}Sr/^{86}Sr$ or $^{143}Nd/^{144}Nd$ in Soufriere rocks and no evidence for significant crustal contamination. The most primitive Soufriere magmas resemble MORB in composition. Any isotopic diversity is restricted to rocks with MgO < 5wt%. St. Vincent is therefore an ideal location to study differentiation or arc magmas without the typical complication of assimilation of older crustal rocks.

EXPERIMENTAL AND ANALYTICAL METHODS

The experimental starting material was selected from the catalogue of St. Vincent whole rock analyses in Robertson (2002). The aim was to find a primitive, Ni-rich, aphyric basalt whose composition could be parental to the differentiation suite of basalts to andesites and whose Mg# (molar Mg/[Mg+Fe$_{tot}$] x100) was at or close to equilibrium with mantle olivine. The selected composition (RSV49; Table 1) is an HMB dyke from Milikin Bay (*South-East Volcanics*, Fig. 1b) with sparse phenocrysts (15 vol%) of olivine (Fo$_{91-76}$) and rare microphenocrysts of clinopyroxene, plagioclase (An$_{80-79}$) and Cr-spinel in a microcrystalline groundmass. RSV49 is close to the composition of another primitive St. Vincent basalt (STV301; Table 1) previously studied experimentally by Pichavant et al (2002) and Pichavant & Macdonald (2007). Compared to RSV49, STV301 is slightly less primitive (Mg# 0.72 versus 0.74) and has higher K$_2$O (0.46 versus 0.28 wt%). Pichavant et al. (2002) studied the phase relations of STV301 with variable amounts of H$_2$O at 0.75 to 2.5 GPa and 1160 to 1290 °C; Pichavant & Macdonald (2007) investigated the hydrous phase relations of STV301 (and a slightly more evolved basalt STV315, Mg# = 0.61) at 0.4 and 1.0 GPa, 1040 to 1200 °C. We consider that the small compositional differences between RSV49 and STV301 impart only minor effects on phase relations enabling us to use some of the experimental data from Pichavant et al. (2002) and Pichavant & Macdonald (2007) to construct phase diagrams and explore parts of parameter space not covered in our study. The different starting H$_2$O contents, 0.6, 2.3 and 4.5 wt%, used in our experiments bracket the range of H$_2$O contents (0.9 -4.0 wt%) in olivine-hosted melt inclusions from primitive St. Vincent basalts (Bouvier et al., 2008), and lie within the range of H$_2$O contents of primitive basalts from other arcs, including the Marianas (Kelley et al., 2010) and Kamchatka (Portnyagin et al, 2007).

RSV49 starting material was prepared from a mixture of oxides (SiO$_2$, MgO, MnO, Al$_2$O$_3$, TiO$_2$, Fe$_2$O$_3$) carbonates (CaCO$_3$, Na$_2$CO$_3$, K$_2$CO$_3$), calcium phosphate and hydroxides (AlOOH and Al(OH)$_3$). The hydroxides were used as a source of H$_2$O; no additional liquid

water was added to the starting material enabling us to maintain very consistent H_2O contents from run to run. The starting composition with 0.6 wt% of H_2O was nominally dry. Its low, but reproducible, H_2O content likely derives from small amounts of adsorbed atmospheric water. Starting materials were doped with selected trace elements at ppm levels in the form of inductively coupled plasma (ICP) standard nitrate solutions, for a simultaneous study of trace element partitioning. The total amount of trace elements added was ~4000 ppm; full trace element partitioning data will be published elsewhere. Starting materials were stored in a box oven at 100°C prior to capsule preparation to avoid any further water gain from the atmosphere. Starting material compositions, based on analysis of glasses fused at high pressure are shown in Table 1.

Phase relations are sensitive to oxygen fugacity (fO_2) as well as pressure (P) and temperature (T). In practice fO_2 is difficult to control in piston cylinder experiments because of the permeability of the capsules and cell materials to hydrogen, which in turn mediates fO_2 through redox reactions involving H_2O, FeO and Fe_2O_3. We adopted an experimental set-up designed to ensure that fO_2 was maintained close to natural levels, estimated by Heath et al. (1998) for St Vincent basalts to be NNO + 0.9 to NNO + 1.8 log units (where NNO denotes the nickel-bunsenite buffer). In order to match approximately the ferric-ferrous ratio of the starting materials to these redox conditions, and thereby minimize H_2O loss or gain during the experiment due to H_2 flux through the capsule walls, the decarbonated, denitrified and trace element-doped mixture of oxides, calcium phosphate and carbonates were pressed into pellets and equilibrated for 2 hours at 1000°C in a CO-CO_2 atmosphere in a vertical quench furnace at an oxygen fugacity corresponding to the NNO buffer. The final step was addition of aluminium hydroxides.

A double capsule technique similar to that described by Hall et al. (2004) and Kägi et al. (2005) was used. An inner $Au_{90}Pd_{10}$/$Au_{80}Pd_{20}$ alloy (2 mm OD) capsule was filled with

approximately 10 mg of starting material, arc-welded shut and placed in an outer Pt capsule (4 mm OD) containing the same starting material (Fig. 2a) in order to minimizes chemical potential gradients in H_2O between inner and outer capsules. To avoid water loss during welding, capsules were frozen with liquid nitrogen. Weight test before and after the welding showed no sign of H_2O loss.

To monitor fO_2 during the experiment an extra Pd capsule (2 mm OD) was placed into outer capsule of some runs (Fig.2a). This capsule was filled with $Ni + Ni(OH)_2$, which breaks down to NiO and H_2O during the run. The solubility of Ni in Pd is sensitive to redox conditions and can be used as an fO_2 sensor (Pownceby & O'Neill, 1994). The mole fraction of Ni in Pd was determined by multiple electron-microprobe measurements. However, careful examination showed that the sensor capsule failed in most, but not all, of our runs and the range of fO_2 in experiments was wider than originally anticipated. The cause of failure was likely H_2O consumption (via H_2 loss) within the sensor capsule, requiring us to develop alternative methodologies to measure fO_2 in run products (see below).

Experiments were curried out in half-inch (12.7 mm) end-loaded piston cylinder apparatus at the University of Bristol at 0.7, 1 and 1.3 GPa and temperature in the range 950 to 1250°C, using $NaCl$-Pyrex-Al_2O_3 assemblies with a friction correction of -3% (McDade et al., 2002). A small amount of BN powder was used to fill the space between crushable alumina sleeve and the capsule, as well as on the top and on the bottom of the capsule. Run durations were 4 to 27 hours, depending on temperature. Temperatures were monitored with $W_{95}Re_5/W_{75}Re_{25}$ thermocouples and are believed to be accurate within ± 10°C. No correction for the pressure effect on thermocouple emf was applied.

To explore phase relations at lower pressures than are attainable routinely in the piston cylinder, two additional experiments were curried out by J.D. Webster in an internally heated pressure vessel (IHPV) at 0.4 GPa at the American Museum of Natural History, New York.

Temperature for both experiments was 1080 °C. The intrinsic fO_2 of the IHPV is about NNO+2, broadly comparable to the piston cylinder experiments (see below).

After quenching capsules were extracted, mounted in araldite resin and polished, first with abrasive paper and then with a series of diamond pastes. Major element compositions of experimental phases were analysed with a Cameca SX100 electron microprobe at University of Bristol. Major elements were calibrated on oxide and silicate standards. To minimize alkali loss during analysis of hydrous glasses we used a 4 nA probe current, 10 μm spot size and a 10 s counting time for alkalis. However, this did not obviate completely the problem, with up to 28% relative Na-loss (from mass balance) in some glasses, notably those with ≥ 6 wt% H_2O. For these runs the microprobe current was dropped further to 2 nA, which fully eliminated Na-loss. Modal proportions of phases were determined by weighted, least-squares regression (Table 2). Calculated Fe-loss/gain does not exceed 6% relative and is unrelated to temperature, H_2O in the glass, or phase assemblage.

H_2O contents of experimental glasses and amphiboles were analysed by secondary ion mass spectrometry (SIMS) at the NERC ion microprobe facility at the University of Edinburgh using a Cameca IMS-4f instrument with nominal 10 kV primary beam of O^- ions. Positive secondary ions were accelerated to 4.5 keV, with offset of 75 ± 10eV to reduce transmission of molecular ions. Beam current was 2-5 nA, resulting in a spot size at the sample surface of ~20 μm diameter. Calibration was carried out on a range of basaltic glass standards with 0 to 4 wt% H_2O (Lesne et al., 2011). The CO_2 contents of experimental glasses in five run products were also analysed by SIMS using same instrument but applying a high mass resolution of 1500 to differentiate between $^{24}Mg^{2+}$ and $^{12}C^+$. Calibration used basaltic glasses with CO_2 contents ≤1.1 wt%.

The $Fe^{3+}/\Sigma Fe$ ratio in glass from 12 runs (Table 2) was measured using Fe K-edge μXANES on the Microfocus Spectroscopy beamline (I18) at the DIAMOND Light Source

synchrotron, UK. I18 uses a Si(111) crystal monochromator which gives an energy resolution of ~1 eV; the energy stability of the beamline is 0.05 eV per day. The beam size at the sample was approximately 2.5 x 4.5 μm. Details are provided as supplementary material (Appendix 1).

EXPERIMENTAL RESULTS

Experimental run conditions, phase assemblages and phase proportion are presented in Table 2, along with relative Fe-loss and aH_2O calculated from the measured H_2O content of the glass following the method of Burnham (1979). Melt and mineral chemistry from each run are reported in Appendix 2. The Fe-Mg exchange coefficients between olivine and melt ($Kd_{ol-melt}$), log fO_2 and fO_2 in log units relative to NNO (ΔNNO) as calculated by a variety of means are presented in Table 3.

Approach to equilibrium

Several factors may inhibit equilibrium in experiments of this type. Gain or loss of volatile components from the capsule via diffusion through the capsule walls; insufficient run durations; temperature gradients; or persistence of unreacted starting materials.

The H_2O concentration in glasses was analysed by SIMS in more than half of the experiments. In all but five (BM6, BM34, BM36, BM24, BM49) there is no H_2O-gain or loss (within analytical uncertainty) relative to starting materials as calculated from mass balance. In two runs, BM16 and BM23, H_2O was measured in the outer capsules (3.65 and 4.36 wt% respectively) and found to be the same, within the error, of the inner capsule values (Table 2), suggesting that any redox caused by H_2 diffusion had reached a steady state over these run durations.

The CO_2 concentration in glass were higher then expected, given that no CO_2 was added to the starting materials. The presence of CO_2 in run products of piston cylinder experiments has

been reported before (e.g. Alonso-Perez et al. 2009, Gaetani and Grove, 1998), and several possible causes have been proposed, including: incomplete degassing of $CaCO_3$ during preparation of starting material; absorption of atmospheric CO_2 onto powdered starting materials; traces of organics left from grinding under ethanol; and carbon diffusion from the graphite furnace. The CO_2 contents of three runs (BM6, BM17, BM9) with durations of 24 hours are 0.65-0.82 wt%. In an experiment (BM16) run for 27 hours the CO_2 content is slightly higher, 0.93 wt%. In contrast, the concentration of CO_2 in a 4-hour experiment, BM23, was only 0.12 wt%; outer capsule glass in the same run contained 0.80 wt% CO_2. The tendency for CO_2 contents to increase with run duration and to be higher in the outer capsule suggests that the main source of CO_2 in our experiments is the graphite furnace, which provides a carbon source for diffusion through noble metal capsules, as previously documented by Brooker et al. (1998). Once carbon penetrates the outer and inner capsules it reacts with Fe_2O_3 to produce CO_2, which dissolves in the melt, and FeO. The net effect of carbon infiltration is therefore to reduce the starting materials slightly, in proportion to the amount of carbon added. Without careful modification of the experimental set-up to eliminate carbon ingress into the capsules, elevated carbon contents are an inevitable consequence of piston cylinder experiments run with graphite furnaces. In our experiments the total amount of carbon added is insufficient to attain volatile saturation in H_2O-undersaturated runs, as evinced by the lack of quenched vapour bubbles. We therefore conclude that CO_2 acts as an inert diluent in our experimental melts, with limited effect on phase relations.

Previous work on hydrous basalts at similar *P-T* conditions has shown that run durations of the order 20 hours (Table 2) are sufficient to reach equilibrium. (e.g, Pichavant et al. 2007; Müntener et al. 2001; Sisson & Grove 1993a, 1993b). Systematic variations in melt composition, melt fraction and mineral assemblages with *P* and *T* in our experiments (see below) are suggestive of a close approach to equilibrium. Observed crystal morphologies

suggest that there were no problems with nucleation and in all but six experiments (RSV49_4, BM24, BM37, BM9, BM58), run products are homogeneously distributed throughout the capsule suggesting a lack of significant thermal gradients across the capsule. A backscattered SEM image of a typical run product is shown in Figure 2b. In three experiments we have crystal-rich and glass-rich parts of the capsule (Fig. 2c) perhaps due to a temperature gradient in these experiments or crystal-settling in hydrous, low-viscosity melts.

In three experiments (BM37, BM9, BM58) clinopyroxene is zoned. This is not unusual in natural rocks or experimental run products (e.g. Skulski et al., 1994; Adam and Green, 1994). In BM37 clinopyroxenes have pronounced sector zoning (Fig. 2d, Tab. 3), very similar to natural clinopyroxene phenocrysts from Grenada (Arculus, 1978), coexisting with homogeneous olivine, spinel and melt. Sector zoning in this run may be the result of a pressure drop of ~ 0.07 GPa overnight. Zoned clinopyroxenes from BM58 and BM9 (Appendix 2) are too small to establish whether zoning is sector or concentric.

Oxidation state of experiments

In Table 2 we present estimates of the redox state of 18 experiments, as ΔNNO, using NiPd sensors and $Fe^{3+}/\Sigma Fe$ in glasses. Calculated fO_2 values based on NiPd sensor are in the range of NNO + 1.0 to - 0.8 for the 15 runs in which a sensor was used. The NiPd sensor estimates rely on the accuracy of the Ni-Pd solubility model, the method used to estimate aH_2O (Burnham, 1979) and, crucially, requires that enough H_2O is present initially to oxidize any Ni in excess of that dissolved in Pd at the experimental fO_2. It is a simple matter to determine by mass balance whether enough H_2O was initially present in the sensor capsule. According to our calculations this was true only in one experiment, bmn1. In the others, insufficient H_2O means that sensor fO_2 always underestimates true fO_2.

The $Fe^{3+}/\Sigma Fe$ ratios in quenched glasses allowed us to calculate fO_2 using the model of Kress and Carmichael (1991). These fO_2 are in the range of NNO - 0.2 to + 4.9and correlate positively with melt aH_2O and negatively with temperature, largely because these two variables are aliased in our H_2O-undersaturated runs. Uncertainties on fO_2 calculated in this way derive from two sources: the μXANES measurements, and the calibration of Kress & Carmichael (1991). Uncertainty on μXANES $Fe^{3+}/\Sigma Fe$ is estimated to be 0.02 to 0.04 (Table 3), which translates to an uncertainty on fO_2 of ±0.4 log units at $Fe^{3+}/\Sigma Fe = 0.50 \pm 0.03$. For glasses with 7 wt% FeO^{tot} the Kress & Carmichael (1991) method leads to uncertainties of similar magnitude. Although Kress & Carmichael (1991) do not include the effect of H_2O various experimental studies (e.g., Botcharnikov et al., 2005) have shown that dissolved H_2O in glasses has negligible effect on $Fe^{3+}/\Sigma Fe$, suggesting that this is not the cause of the apparent $Fe^{3+}/\Sigma Fe$ versus aH_2O correlation.

In two experiments, BM6 and BM34 the $Fe^{3+}/\Sigma Fe$ ratio was measured in both the inner and outer capsules. In BM34 the values agreed within error (Table 3), whereas in BM6 $Fe^{3+}/\Sigma Fe$ in the outer capsule is considerably higher. The same run shows a water gain in the inner capsule compared to the mass balance value (Table 2) suggestive of H_2 ingress, leading to reduction.

We conclude that the most reliable fO_2 estimates for our experiments are NNO + 2.6 ± 1.4 (μXANES method; Fig. 3). This is somewhat more oxidizing than the experiments of Pichavant et al. (2002) and Pichavant & Macdonald (2007) (NNO + 0.7 ± 1.0), but at the upper end of the range of natural St Vincent basalts as calculated by Heath et al. (1998) using the olivine-spinel oxybarometer of Ballhaus et al. (1991): NNO -0.1 to +0.9 (Fig.3). We applied the same oxybarometer to the dataset of Robertson (2002) and obtained fO_2 values for

basalts in the range NNO +1 to +1.4, and in basaltic-andesites and andesites from NNO + 2.3 to + 4.3 (Fig.3).

Phase Equilibria

Phase diagrams for the experimental series with different H_2O contents are shown in Figure 4. For brevity we refer to the 0.6 wt% H_2O experiments as "dry"; those with 2.3 wt% as "damp" and those with 4.5 wt% as "wet". We have supplemented our data with results from Pichavant et al (2002) and Pichavant & Macdonald (2007) on STV301 (Table 1). These studies did not fix the amount of H_2O in their bulk compositions. Thus comparisons have only been made for comparable (i.e. ±10% relative) bulk H_2O contents, as calculated from their analysed glass H_2O and mass balance. Even in those cases where the H_2O contents are similar, the experimental fO_2 may differ by up to 2 log units and this should be borne in mind when comparing the results. Changes in fO_2 principally affect the liquidus stability of spinel and the *Fo* content of olivine (Stamper et al, 2014).

Dry (0.6 wt% H_2O).

The dry phase diagram is limited to a single pressure (1 GPa), augmented by an experiment at 1.3 GPa from Pichavant et al. (2002), which helps delineate the olivine-out phase boundary. The 1 GPa liquidus is at approximately 1300 °C. There are narrow (<80 °C) sub-liquidus cumulate fields of first dunite and then harzburgite. This is the only experimental sequence to generate harzburgite (i.e. orthopyroxene + olivine) residues. Olivine reacts out at 1230 °C, simultaneously with the appearance of plagioclase. The principal cumulate assemblage at temperatures below 1240 °C is gabbronorite. The 1.3 GPa experiment (#23) of Pichavant et al. (2002) produces websterite cumulates at 1230 °C, consistent with expansion of the clinopyroxene stability field at higher pressures.

Damp (2.3 wt% H_2O).

Liquidus temperatures in the damp series were not defined. According to the parameterisation of Médard and Grove (2008) they will lie ~60 °C lower than the dry series at all pressures and have been shown accordingly in Fig. 4. The liquidus assemblage is olivine + spinel at 0.7 GPa and we consider this to be likely at all other pressures studied, defining a narrow near-liquidus cumulate assemblage of dunite. At 1 GPa dunite persists until the appearance of clinopyroxene at 1180 °C. A broad field of wehrlite stability follows with decreasing olivine:clinopyroxene ratios to lower temperatures, terminated by the simultaneous disappearance of olivine and appearance of orthopyroxene at 1080 °C to produce a websterite assemblage. Olivine-out occurs at higher temperature (>1150 °C) at 1.3 GPa and lower temperature (1050 °C) at 0.7 GPa, such that the wehrlite field broadens with decreasing pressure, whereas the websterite field broadens with increasing pressure. This is consistent with the experimental results of Müntener et al. (2001) on a primitive basalt from the Cascades. Hornblende appears at ~1050 °C at 1 and 0.7 GPa, but is absent in a 0.4 GPa experiment at 1080 °C; its stability at 1.3 GPa has not been determined, although we note that at 1.2 GPa Müntener et al. (2001) find that hornblende appears between 1100 and 1070 °C for a slightly higher bulk H_2O content. Pichavant & Macdonald (2007) do not find hornblende in any of their 0.4 GPa experiments, regardless of H_2O content, suggesting that hornblende saturation defines a minimum pressure in hydrous primitive basalts. The cumulate assemblage at and above 0.7 GPa is hornblende pyroxenite, whose stability field is terminated by the appearance of plagioclase at 950 °C at 1 GPa, 1000 °C at 0.7 GPa, and 1050 °C at 0.4 GPa (Pichavant & Macdonald, 2007). The resulting hornblende gabbronorite assemblage defines the low temperature extreme of our phase diagram, with increasing proportions of hornblende and plagioclase down-temperature. Olivine is only stable, at the expense of hornblende, below 0.7 GPa, forming olivine gabbronorite cumulates.

Wet (4.5 wt% H_2O).

The wet phase diagram shares some topological similarities with the damp phase diagram. There is a near-liquidus field of spinel, but the liquidus itself is not defined; according to the parameterization of Medard and Grove (2008) it should be depressed by about 50 °C compared to damp experiments and is shown accordingly in Fig. 4. In terms of cumulate assemblages, the dunite field broadens down-pressure, followed by a broad field of wehrlite. Olivine stability is enhanced and orthopyroxene suppressed compared to the damp case, such that websterite is displaced to a narrow region above 1 GPa. A single experiment at 1150 °C and 1.3 GPa produced an olivine-websterite assemblage within ~50°C of the liquidus. Hornblende appears at progressively lower temperature with increasing pressure, from 1100 °C at 0.7 GPa to 1050 °C at 1.3 GPa. Hornblende is lacking at 0.4 GPa, consistent with Pichavant & Macdonald (2007). At higher pressures cumulates are olivine-pyroxene hornblendite and hornblende pyroxenite. The persistence of olivine and absence of orthopyroxene in a single experiment (BM24) at 1 GPa and 1030 °C is curious, suggesting a sharp backbend in the olivine-out/orthpyroxene-in curves at intermediate pressures. Plagioclase is entirely absent from the wet phase diagram, as also noted by Pichavant & Macdonald (2007), thus no cumulate gabbros or gabbronorites occur in the *P-T* region studied. We suggest that these would be near-solidus assemblages for our wet basalts. Given the dearth of orthopyroxene and persistence of olivine in wet basalts, olivine hornblende-gabbro is the most likely such assemblage.

In summary, cumulate assemblages are very sensitive to *P, T* and initial H_2O content. For all basalts there is a narrow liquidus field of spinel-bearing dunite. For hydrous basalts wehrlite has a broad stability field, becoming hornblende pyroxenite below ~1050 °C above 0.4 GPa. Websterites are confined to higher pressures; gabbronorites, with or without olivine and hornblende, are confined to lower pressures and bulk H_2O contents. Harzburgites are rare, confined to a narrow stability field for relatively dry basalts. A single wet run (BM49) at 1.3

GPa and 1150 °C was in equilibrium with olivine, orthopyroxene, clinopyroxene and spinel, consistent with derivation from mantle wedge peridotite. This supports the conclusion of Pichavant et al. (2002) that St. Vincent MgO-rich basalts can be derived from a peridotite source; they infer multiple saturation for STV301 with 4.5 wt% H_2O at 1.6 GPa and 1185 °C.

Melt Fraction

Phase proportions change systematically with P, T and bulk H_2O content (Table 2; Figure 5). As we have not determined the solidus temperature in our experiments this has been extrapolated from the H_2O-saturated solidus in the haplogranite system (Johannes & Holtz, 1996). The point of H_2O saturation is marked by the appearance of large vapour bubbles in some run products, as noted in Table 2. As previously described by Melekhova et al (2013) melt fraction (F) shows non-linear variation with temperature for dry experiments at 1GPa, damp experiments at 0.7 and 1 GPa and wet experiments at 0.7 GPa; the relationship becomes more linear for damp experiments at 1.3 GPa and for wet experiments at 1.0 and 1.3 GPa. By comparing experiments at fixed pressure (1 GPa) and variable H_2O we see that the F-T relationship becomes more linear with increasing H_2O. For fixed initial H_2O, linearity increases with increasing P. The most extreme variation in F with T is seen in 1 GPa, dry experiments with F decreasing from 0.95 to 0.35 over just 20 °C. For the wet system at 1 GPa the same crystallization interval takes place over almost 200 ºC. For a given T and starting composition F both decreases and increases with decreasing pressure. However the exact relationship is non-linear and varies with H_2O content.

In detail the F-T relationships are a consequence of the changing crystallising assemblages (Melekhova et al, 2013). The effect of amphibole crystallization on melt production has been previously recognized (e.g. Holloway & Burnham, 1972; Grove et al. 1997; Barclay & Carmichael, 2004, Davidson et al, 2007). In Figure 5 we indicate changes in crystallizing assemblage with changing T. It is immediately apparent that amphibole is not the sole reason

for the observed rapid change in F. In several experimental sequences, notably the 1 GPa, amphibole-free dry experiments, it is the peritectic reaction olivine + melt = orthopyroxene that heralds the most abrupt change in crystallization rate (dF/dT). In all experiments where amphibole is present its appearance occurs *within* the period of maximal dF/dT, rather than at the onset.

The principal control on F-T relationships is compositional contrast between the crystallizing assemblage and the coexisting melt. Rapid changes in F occur during eutectic-like behavior, i.e. melt and crystalline residue have similar composition. Conversely, during peritectic reaction small changes in F can lead to large change in melt composition. For example, orthopyroxene and plagioclase are compositionally similar to basaltic melts and an abrupt decrease in F would be observed on saturation with these minerals (Villiger et al, 2004, 2007), consistent with the maximum dF/dT observed when orthopyroxene and plagioclase appear in dry experiments at 1 GPa (Fig. 5). In contrast, amphibole and melt differ greatly in composition and lower dF/dT is observed upon amphibole saturation in the wet basalt at 1 GPa (Fig. 5). However, change in melt composition is substantial (BM37-BM34). For the damp basalt, both amphibole and orthopyroxene appear simultaneously, making dF/dT intermediate between dry and wet cases.

Phase Compositions

Olivine

Olivine forms homogeneous large euhedral to subhedral prisms up to 200 μm across and small rounded crystals down to 10 μm. Olivine composition changes from Fo_{94} to Fo_{86} (Fig. 4), generally decreasing with decreasing temperature. However, this is not true for all of our experiments, emphasising the dual role of T and fO_2 in controlling Fo (Stamper et al, 2014). At the point of near-multiple saturation with a lherzolitic assemblage (run BM49) olivine is

Fo$_{93}$, in good agreement with the 1.6 GPa multiple saturation point of Pichavant et al (2002): Fo$_{92}$.

It is widely accepted that exchange coefficient (Kd) for Fe^{2+} and Mg between melt and coexisting olivine of 0.3 ± 0.03 is an indication of equilibrium conditions for a wide range of temperatures and compositions (Roeder & Emslie, 1970). However, Kd is influenced by Fe^{3+}/ΣFe and where there is significant Fe^{3+} the *apparent* Kd (i.e. taking all Fe as Fe^{2+}, as usually assumed) will be reduced. For those experiments in which we have used µXANES to determine Fe^{3+} the *true* Kd varies from 0.28 to 0.52 (mean = 0.38 ± 0.07) (Table 3). This is clearly higher than the canonical value, but there is reasonable agreement between our values and those calculated by the method of Toplis (2005) for the same runs: 0.33 to 0.46 (mean = 0.37 ± 0.04). Although small discrepancies between our values and those of Toplis (2005) may reflect a failure to achieve equilibrium, we note that his method does not include any explicit term for Fe^{3+} in the melt and this component may also influence Kd. In this context it is worth noting that Pichavant & Macdonald (2007) obtain Kd's for their 15 olivine-bearing runs, after correction for Fe^{3+} using the method of Kress & Carmichael (1991) in the range 0.28 to 0.36 (mean = 0.31 ± 0.03). Matzen et al (2011) in a study of olivine-melt equilibria at 1 atmosphere find a mean Kd of 0.345 ± 0.009, although again their Fe^{3+} contents are calculated, rather than measured by µXANES. For a more extensive database they arrive at a mean Kd ≈ 0.34, i.e. somewhat higher than the canonical value. They warn that, "application of constant Kd$_{Fe-Mg}$ values to highly oxidizing systems should be approached with caution". We conclude that olivine-melt Kds cannot be used as evidence for or against equilibrium in relatively oxidized runs.

In terms of minor elements, the CaO content of olivine reaches 0.49 wt% and shows a weak positive correlation with temperature. Olivine NiO contents range from 0.82 to 0.09 wt%. There is no clear correlation between Fo content of olivine and minor elements, but

there is a positive correlation between NiO content of olivine and coexisting spinel (Appendix 2).

Spinel

Spinel is the first liquidus phase to appear and is present in every experiment often occurring as an inclusion in other phases, particularly olivine. The grainsize of near-liquidus spinel is very small, in some cases less than 1 μm, making it impossible to analyze. In the cases when analyses were not possible the chemical composition of spinel from a nearby experiment was used for mass balance calculations (Table 2). Spinel grainsize of increases down temperature reaching a maximum of 10 μm at 1000 °C.

Compositions range from Cr-Al spinel at high temperature through Al-rich spinel (pleonaste) to high Al magnetite in "damp" and titanomagnetite in "wet" experiments at lower temperature, in good agreement with the data of Pichavant & Macdonald (2007) and Pichavant et al. (2002). In "dry" experiments pleonaste + ilmenite occur in place of magnetite. The dominant control on spinel chemistry was found to be melt composition, as reflected in the melt fraction, F (Fig. 6). $Cr\#$ (=Cr/[Cr+Al]) decreases as crystallization proceeds (Fig. 6a). The highest Cr# spinels are found close to the liquidus in experiments of Pichavant et al (2002) with melt H_2O in the range 1-2 wt%, at 0.7 to 1.5 GPa. In our experiments $Cr\#$ decreases discontinuously with decreasing F, creating a small compositional gap between $Cr\#$=0.1 and 0.2. This gap reflects the sudden change in melt composition due to high dF/dT (Fig. 7; Melekhova et al 2013) and consequently is widest for dry experiments.

$Al\#$ (=Al/[Al+Fe^{3+}+Cr]) shows three distinct trends (Fig. 6b). The first involves an increase of $Al\#$ with decrease of F independent of P or initial H_2O content. Dry experiments (ours and those of Pichavant et al (2002)) and experiments at 0.4 GPa by Pichavant and Macdonald (2007) have the highest $Al\#$ at high F. The other two trends indicate a reversal in Al

partitioning into spinel, such that *Al#* decreases with decreasing *F*. The reversal coincides with the onset of hornblende + plagioclase co-precipitation in damp experiments and the appearance of hornblende in wet experiments.

In terms of *Fe#* (= Fe^{2+}/[Fe^{2+}+Mg]), there is a small increase with decreasing *F*, reaching a maximum at the onset of magnetite crystallization. TiO_2 content is generally low, only increasing when magnetite appears.

On Figure 6c and d we show *Cr#* and *Al#* as functions of ΔNNO for experiments analysed by μXANES (Table 3). Our data are compared to the experimental results of Pichavant & Macdonald (2007) who used an Ni-Pd sensor to determine fO_2. There is a remarkable agreement between the two datasets at comparable ΔNNO. *Cr#* barely changes below ΔNNO +1.5 then drops very rapidly with increasing fO_2 (Fig. 6c). A similar correlation between *Cr#* and fO_2 was observed by Roeder (1991). Al# has a negative correlation with fO_2, decreasing steadily until ~ ΔNNO +3 (Fig. 6d). The subsequent drop in *Al#* in our wet experiments is due to magnetite crystallization.

For experiments with coexisting olivine and spinel we calculated fO_2 following O'Neill & Wall (1987). These range from NNO - 0.4 to +4.0 (Table 3). For the runs which were analysesd by μXANES the two methods of calculating fO_2 show some coherence, especially at high fO_2, but discrepancies are up to 2 log units for the more reduced runs. Uncertainty in olivine-spinel oxybarometry derives from uncertainty in the thermodynamic calibration (estimated to be ± 0.8 log units by O'Neill & Wall (1987)) and from assumptions made about the activity of orthopyroxene, which is not present in any of the runs for which we know Fe^{3+}/ΣFe. We used an average enstatite activity of 0.75, which imparts a further uncertainty of ± 0.5 log units.

Pyroxenes

Clinopyroxene shows a wide variation in crystal size (150 to 10 μm), which appears unrelated to T, P or H_2O. Clinopyroxenes are aluminous augites (≤9.7 wt% Al_2O_3) with the exception of diopside in bmn1. TiO_2 contents are in the range 0.2 to 0.7 wt%. A single low Al, low Ti clinopyroxene was observed in BM58. The average $Fe^{3+}/\Sigma Fe$, as calculated by stoichiometry, is 0.12. The dominant exchange vector is tschermakite (Fig.7a) with almost all Al, Fe^{3+} and Ti on M1 sites charge-balanced by tetrahedral Al.

Clinopyroxene composition is controlled by a variety of factors, including P, T, fO_2 and the composition of the melt, which in turn is influenced by F and the nature of co-precipitating phases. It is consequently difficult to ascribe changes in clinopyroxene composition to a single variable. Ca serves as a case in point. The Ca content of clinopyroxene has a strong correlation with F, T, melt H_2O content, and P. Ca increases with melt H_2O (e.g., Gaetani et al., 1993, Müntener et al., 2001, Di Carlo et al., 2006), decreasing T (Fig. 7b) and decreasing P (Fig. 7c). Amphibole crystallization has no affect on Ca content of coexisting clinopyroxene.. There is no systematic variation of Al or Na with T in our experiments (e.g., Müntener et al., 2001; Gaetani and Grove, 1998), although there is a positive correlation between Na and P (Fig. 7d).

Orthopyroxene forms small equant grains 10-15 μm in diameter. Orthopyroxenes are enstatite with high Al_2O_3 (6-10wt%); the dominant exchange vector is tschermakite. There is no systematic variation in Ca, Al or Na in orthopyroxene with magmatic parameters, although there is a small increase of TiO_2 content in orthopyroxene with decreasing T (Appendix 2).

Amphibole

Amphibole forms euhedral crystals up to150 μm across. Amphiboles are Tschermakitic hornblende (Leake et al., 1997), with the exception of magnesiohastingsite in BM39, with 13.3 to 15.6 wt% Al_2O_3, Mg# of 74 to 80 and 5.9 to 6.2 Si atoms per formula unit (apfu).

Mg# decreases with decreasing temperature and correlates negatively with Al (Fig. 8a) consistent with increasing Al as crystallization proceeds, as previously noted for spinel. The sudden drop in Al at low Mg# (Fig. 8a) is caused by the onset of plagioclase crystallization. Ti contents are in the range 0.09 to 0.16 apfu and have a positive correlation with Mg# in both damp and wet series although the trends are displaced to higher Ti at lower H_2O (Fig. 8b). A single amphibole from Pichavant & Macdonald (2007) in an experiment with 2.7 wt% initial H_2O lies closer to our wet rather than damp trend (Fig. 8b).

Plagioclase

Plagioclase was observed only in the damp and dry series of experiments. *An* content ranges from 81 to 60 mol% in damp experiments and 58 to 49 mol% in dry experiments, in both case decreasing systematically with decreasing *T* (Fig. 4). The higher *An* contents in damp experiments relative to dry experiments reflect the well-known tendency of H_2O to suppress the plagioclase liquidus.

Melt

Glass compositions were analyzed in all experimental run products but two, BM60 and BM56, due to small glass pools and abundant quench crystals respectively. For the mass balance calculations in these runs average melt composition of the nearest temperature experiments were applied. In some run products patches of quench material are present, typically as quench crystals nucleated around spinel. Quench proportions correlate with melt H_2O content. However, very low residuals of mass balance calculations demonstrate that the presence of quench crystals does not modify melt composition significantly. Experimental melts show an extensive range in composition from high-MgO basalt through andesite to rhyolite (Appendix 2, Fig. 9). SiO_2 contents are inversely correlated with *F*, as expected,

however in detail the relationship depends on bulk H_2O content because of the changing crystallizing assemblages.

Despite the variability of mineral chemistry there is a remarkably systematic variation of melt composition with T (Fig. 10; Appendix 2). There is a very good agreement between experimental glasses from this study and those from Pichavant & Macdonald (2007) and Pichavant et al. (2002) for all major elements except K_2O and TiO_2 due to the higher initial content of K_2O and TiO_2 in STV301 (Table1). Consequently, for these two oxides comparison of our data to those of Pichavant & Macdonald (2007) and Pichavant et al. (2002) is not meaningful and they are not presented on Figure 10.

There is an increase in melt SiO_2, Na_2O, K_2O (Fig. 10a, b, c), with decreasing T and opposite behavior of MgO and Cr_2O_3 (Fig. 10d, e). SiO_2 shows a non-linear relationship with T, due to the changing SiO_2 content of the bulk crystal residues with different experimental conditions. A striking feature is the abrupt increase in SiO_2 in melts from the damp experiments at T below 1030 °C due to copious precipitation of low-SiO_2 amphibole. Amphibole also saturates at low temperatures in the wet experiments, but we have insufficient low T data to see the same abrupt rise in SiO_2. K_2O correlates inversely with F, which, in turn, is controlled by initial H_2O and T (Fig. 10c).

Cr_2O_3 drops sharply at high temperatures due to precipitation of Cr-rich spinels (Fig. 10e). Scatter results from variation in fO_2 between different experiments, influencing the total magnetite content of the spinels. FeO_{total} is controlled by a combination of mafic minerals and magnetite, saturation of which triggers the marked decrease in concentration below ~1050 °C (Fig. 10f). Al_2O_3, CaO and TiO_2 (Fig. 10g, h, k) are characterized first by an increase with decreasing T, followed by a decrease as different hosting phases saturate in the melt. Al_2O_3 climbs sharply until saturation of plagioclase, which occurs at progressively lower T with increasing initial H_2O and increasing P (Fig. 5). Consequently the maximum in Al_2O_3 content

is a strong function of basalt H_2O content (Pichavant & Macdonald, 2007). CaO is driven largely by clinopyroxene $\pm$ plagioclase (Fig. 5). The earlier saturation of clinopyroxene and plagioclase in dry experiments, compared to damp and wet experiments, accounts for the near monotonous decrease in CaO with temperature. A delay in clinopyroxene saturation, as seen for some of our damp and wet experiments and those of Pichavant & Macdonald (2007), leads to production of Ca-rich melts. As a consequence, the relative appearance of clinopyroxene leads to two different evolutionary series to high and low CaO (Fig. 10h).

TiO_2 also shows two distinct trends, labeled "F" and "magnetite" in Figure 10k, governed respectively by the combined effects of melt fraction and Ti-phase saturation. At high T the increase in TiO_2 is controlled by melt fraction, which is lower at a given temperature in the dry runs, hence the steeper increase. This is enhanced further by the lack of amphibole in these runs, and TiO_2 reaches the highest concentration in the dry experiments at 1130 °C (~1.8 wt%), dropping thereafter due to the appearance of ilmenite. In the damp and wet experiments magnetite crystallization causes a significant drop in TiO_2 below ~1100 °C.

Melt evolution in terms of tholeiitic versus calc-alkaline differentiation trends is shown in Figure 11. Melts from all series of experiments follow an initial tholeiitic trend to increased FeO/MgO, followed by an inflection at SiO_2 above ~52 wt% that takes them into the calc-alkaline field. The inflection can be ascribed to the onset of magnetite (wet and damp series) or ilmenite (dry) crystallization. The single experiment of Pichavant & Macdonald to plot in the calc-alkaline field (Fig. 11) is also magnetite-saturated. Although the appearance of an Fe-Ti oxide phase is partially controlled by fO_2 this is not the only factor; melt fraction also plays an important role, as noted in the discussion of spinel chemistry. This is apparent from Figure 11 where fO_2 from some of our experiments and those by Pichavant and Macdonald (2007) is indicated, showing clearly that there is no simple correlation between fO_2 and tholeiitic or calc-alkaline character.

COMPARISON TO NATURAL ROCKS

One objective of this study is to assess the extent to which mid to lower crustal crystallisation of mantle-derived basalts can generate the observed compositional diversity of lavas, phenocrysts and plutonic xenoliths on St. Vincent.

Melt Compositions

In Figure 12 (a-g) glass compositions from our experiments and those of Pichavant & Macdonald (2007) and Pichavant et al. (2002) are compared to whole-rock analyses of St Vincent lavas (Heath et al, 1998a; Robertson, 2002), melt inclusions (Heath et al., 1998a; Bouvier et al., 2008) and cumulates (Tollan et al 2012). Heath et al. (1998a) provided data on melt inclusions from all main phenocrysts phases, whereas Bouvier et al. (2012) present analyses of melt inclusions hosted by olivine (Fo_{90-86}), which they corrected for post-entrapment crystallization. Tollan et al. (2012) analysed glassy melt inclusions in two cumulates xenoliths, sample VS36 (Fo_{76} host) and VS3-2 (hornblende host), without correction for post-entrapment crystallisation. Experimental starting compositions, RSV49 and STV301 are also shown in Figure 12. Sequential melts from 0.7 GPa damp experiments are connected by a solid line to illustrate their chemical evolution. MgO is plotted on the abscissa because it shows greater variation than SiO_2.

The striking feature of Figure 12 is the extent to which our experimental melts bracket the entire compositional spectrum of St. Vincent lavas for all components with the exception of FeO_{total}. Comparisons between experimental and natural melts enable us to draw some inferences about the conditions under which the natural compositional variation was generated.

A notable match between experiments and lavas comes for Al_2O_3 (Fig. 12b), where we are able to generate the high-alumina (>20 wt%), low-MgO (<4 wt%) basalts and basaltic

andesites found on St. Vincent via crystallization of wet parent basalts. The melts that have these characteristics (bmn2 and BM50) have ≥ 8.3 wt% H_2O dissolved in the melt. This value is equivalent to saturation at pressures of 0.4 GPa, thereby providing a minimum pressure estimate for generation of high-alumina compositions from high-MgO parents. At lower pressures H_2O contents would be limited by lower solubility, plagioclase saturation would occur at higher temperatures and Al_2O_3 enrichment would be suppressed. Similarly, the high TiO_2 contents (Fig. 12c) observed in the dry series of experiments exceed those observed in most St. Vincent lavas, suggesting that the parent basalts typically did not have such low H_2O contents, in accord with melt inclusion data (Bouvier et al., 2008).

The principal exception to reproducing natural compositions is FeO_{total} (Fig. 12d), which extends to higher values below 6 wt% MgO than our experimental glasses. The experimental melts have high $Fe^{3+}/\Sigma Fe$, which will tend to favor early magnetite saturation, driving residual melts to lower FeO_{total}. This is apparent from Figure 11 where we show that magnetite-saturated melts are displaced to lower FeO_{tot}/MgO. The three magnetite-saturated, damp experiments from Fig. 11 are enclosed in the dashed ellipse on Figure 12d to show the consequences of early magnetite saturation. As magnetite saturation is largely a function of fO_2 it is likely that the delayed saturation of this phase on St. Vincent is a consequence of the slightly lower fO_2 of the lavas compared to the experiments.

Alkali contents of melts are very sensitive to F and crystallizing assemblages. Extensive crystallization of amphibole with around 16 wt% MgO and 2.5 wt% Na_2O in our wet and damp experiments serves to limit the increase in Na_2O (Fig. 12e), however amphibole alone cannot explain the marked inflection in Na_2O below 6 wt% MgO which requires extraction of a phase with >4 wt% Na_2O. The logical candidate phase is plagioclase, which, in the damp experiments has around 2-5 wt% Na_2O and negligible MgO, such that co-precipitation of amphibole and plagioclase would drive residual melts to lower MgO and Na_2O. Another

possibility is that Na_2O partitions into the coexisting vapour phase. A single, vapour-saturated wet experiment (indicated on Fig. 12e) supports this suggestion. Notably melt inclusions show the same trend to low Na_2O below 4 wt% MgO.

The high K_2O content of STV301 (used by Pichavant et al., 2002 and Pichavant & Macdonald, 2007) results in much higher K_2O in their experimental melts compared to lavas. The principal control on K_2O is *F*. Our wet (high *F*) and dry (low *F*) experiments diverge below ~10 wt% MgO to bracket upper and lower bounds of the lavas. The dramatic increase in K_2O in the damp experiments at 0.7 GPa (solid line on Fig. 12f) reflects extensive crystallization of amphibole and plagioclase. Some lavas are also displaced to high K_2O at low MgO, plausibly due to the same process, although we cannot rule out variability in parental K_2O or magma mixing between dry and damp/wet basalts on St. Vincent.

The experimental melts produce two distinct trends for CaO (Fig. 12g) due to the early or late onset of clinopyroxene crystallization. Stamper et al (2014) have shown similar behavior for the case of Grenada, where they attribute the origin of the CaO-rich "C-series" lavas (Arculus, 1976; Hawkesworth et al, 1979) to shallow crystallization and the CaO-poor "M-series" lavas to higher pressure crystallization. Although St. Vincent does not show discrete M- and C-series differentiation trends, it is interesting that olivine-hosted melt inclusions (Bouvier et al., 2008) are very CaO-rich, a feature that Bouvier et al. (2008) attributed to magma interaction with a CaO-rich, amphibole-bearing lithology. Conversely, our experimental results, and those of Stamper et al. (2014) and Pichavant & Macdonald (2007), show that such CaO-rich melts could equally well be produced from crystallization of high MgO basalt at $\leq$0.7 GPa. Bouvier et al's (2008) high-CaO melt inclusions are hosted by olivines with Fo_{87-90}, as found in our experiments with the highest CaO glasses (Fo_{90}). It is unclear why there are CaO-rich melt inclusions, but no CaO-rich lavas, on St Vincent.

Mineral Compositions

In this section we compare experimentally-produced mineral compositions, from this study plus Pichavant & Macdonald (2007) and Pichavant et al. (2002), to compositions of phenocrysts from St Vincent lavas and minerals from plutonic xenoliths (Lewis, 1973a, b; Robertson, 2002, Tollan et al., 2012, Bouvier et al., 2008). In contrast to the good match between experimental glasses and erupted lavas, the overlap between experimental and natural crystal assemblages is poor.

Olivine

Olivine phenocryst compositions are presented in Figure 13. In general the CaO content of olivines increases with decreasing Fo, however, three discrete groupings are apparent. Olivines from lavas define trends of high and low CaO, spanning Fo_{90-71} and Fo_{92-56} respectively. The high CaO trend comprises HMB; the low CaO trend LMB, BA and andesites and plutonic olivines. Experimentally-produced olivines form a third grouping at even higher CaO, with a more limited range of Fo_{94-80}. No experimental olivines lie in the low-CaO phenocryst field; and only four (one from this study, three from Pichavant & Macdonald 2007) lie within the high-CaO field. These are exclusively olivines produced in experiments at 1030-1050 °C from basaltic melts with high H_2O (6 to 8.4 wt%) and MgO in the range 3.9 to 7.2 wt%. Melt inclusion-hosting olivines from Bouvier et al. (2008) lie at the high-Fo extremity of the high-CaO phenocryst field, consistent with their CaO-rich melt compositions, and overlap those of the experiments. A cluster of Ca-poor olivines ($Fo_{86-91,}$) from HMB have CaO (<0.06 wt%) and NiO (0.29 – 0.50 wt%) contents similar to mantle peridotite xenoliths from Grenada (Parkinson et al 2003), and may represent entrained xenocrysts from the mantle source region.

The discrepancy in CaO contents of experimental olivines compared to natural olivines suggests that phenocrysts and plutonic blocks crystallized under conditions different to those in the experiments. Olivines from H_2O-rich basaltic experimental melts lying within the CaO-

rich phenocryst field suggest that some HMB may have been generated under conditions of relatively low temperature ($\leq$1050 °C) and high H_2O content. For all other phenocrysts, no direct match to individual experimental compositions can be made, despite the fact that experimental melts are a close match to lavas (Fig. 12). This paradox can be reconciled if we consider phenocrysts to be the products of relatively low pressure crystallization of melts produced at higher pressure conditions similar to those of experiments. Shallow crystallization may occur when ascending melts stall in the crust or reach their H_2O-saturated liquidi at low pressures. Low pressure, hydrous basaltic and andesitic magmas invariably have olivine as the principal liquidus phase. Thus we can make a distinction between the mineral compositions that drive deep-seated differentiation and those that precipitate from derivative melts within the shallow crust. Plutonic olivine Fo and CaO contents are consistent with crystallization from melts similar in composition to LMB, BA and andesites, i.e. relatively evolved compositions, at low pressures, as previously suggested by Tollan et al. (2012). Only the melt inclusion-hosting olivines from scoria have compositions consistent with relatively deep-seated fractionation and they may be the only mineral relics of this episode preserved in St. Vincent lavas. In all other cases phenocrysts are exclusively shallow in origin, with the possible exception of some putative mantle xenocrysts.

Spinel

There is a continuum of spinel compositions in St Vincent lavas from Cr-spinel to titanomagnetite, although there is some bimodality in $Fe^{3+}\#$ ($Fe^{3+}/(Fe^{3+} + Cr + Al)$), $Cr\#$ and TiO_2 (Fig. 14a, c and d), which is not unusual for island arcs (e.g. Barnes & Roeder, 2001). Spinels from plutonic xenoliths are strongly bimodal with a group of Al-rich spinels of low $Cr\#$ and intermediate $Fe^{2+}\#$ ($Fe^{2+}/[Fe^{2+}+Mg]$) and a second group of low Al and Cr magnetites (Fig. 14a-d). Spinel associated with melt inclusions (Bouvier et al., 2008) is Al-rich with $Cr\#$ decreasing from 0.7 to 0.02, and low $Fe^{2+}\#$ (0.2 - 0.4).

Experimental and natural spinels show a good match in terms of $Al\#$ (Fig. 14a). The $Al\#$ of spinel from lavas is displaced to lower values (Al#≤0.4) compared to spinels associated with melt inclusions (Al#≤0.9) or plutonic xenoliths (Al#≤0.68), although the latter also contain a discrete population of low-Al# spinels similar in composition to phenocrysts. Three near-solidus damp experiments (BM58, BM52, BM15) also crystallized magnetite compositionally similar to the spinels from lavas and xenoliths. Spinels from RSV49 are lower in Al# and higher in $Fe^{2+}\#$ compared to experiments, but resemble some xenolith spinels. TiO_2 contents of experimental spinels describe a curved trajectory from low TiO_2 at low $Fe^{2+}\#$ to Ti-magnetites at high $Fe^{2+}\#$ similar to spinels from lavas and plutonic xenoliths (Fig. 14b).

The $Fe^{3+}\#$ of experimental spinels increases with increasing $Fe^{2+}\#$ (Fig. 14c). The positive correlation between $Fe^{3+}\#$ and $Fe^{2+}\#$, along a vector towards magnetite, is observed also for natural spinel. The displacement of experimental spinels to higher $Fe^{3+}\#$ compared to lavas and xenoliths likely reflects the higher fO_2 of the experiments; Pichavant & Macdonald's spinels from slightly lower fO_2 conditions provide a better match to nature. We illustrate this effect schematically in Figure 14c.

The Cr# of experimental spinels is consistently lower than spinel from lavas, with a maximum of 0.50 in our damp experiment at 0.4 GPa and 0.45 in an experiment (7-2) of Pichavant & Macdonald (2007) at the same P (Fig. 14d). The only good match is between spinels in our wet experiments and spinels from a plutonic xenolith analyzed by Tollan et al. (2012). The tendency of lower pressure experiments to provide a better match to spinels from lavas and the requirement for protracted plagioclase crystallization to drive up Cr# (Fig. 14c) suggests that pressure may exert a strong influence on Cr#-$Fe^{2+}\#$ systematics, such that high-Cr# spinels from lavas crystallised at lower P than the experiments. Such a possibility could be tested with a set of atmospheric pressure experiments.

Pyroxene

Clinopyroxene phenocrysts have a wider range of Mg#$_{92-56}$ compared to experiments (Mg#$_{88-74}$) and plutonic xenoliths (Mg#$_{82-72}$) but a similar range in Ca content (Fig. 15a). The spread in phenocryst Mg# is most likely an indication of crystallization from melts ranging from HMB to andesites. The Ca content of phenocrysts is positively correlated with Mg#, and xenolith clinopyroxenes lie close to the high Mg# extremity of this trend. Experimental clinopyroxenes extend away from the xenoliths to lower Ca, with high temperature (1200-1180 ºC) experiments showing the lowest Ca contents. The experiments that provide the best match for phenocrysts are those at $T \leq 1100$ ºC, $P \leq 0.7$ GPa, and $H_2O \geq 2.8$ wt%.

Orthopyroxene is rare in xenoliths but widespread in lavas. Experimental orthopyroxenes have Mg# considerably higher than natural phenocrysts (Fig. 15b,c) indicating that phenocrysts grew from more evolved melts. Natural orthopyroxenes are lower in Al^{iv} than most experimental orthopyroxenes (Fig. 15b) again consistent with lower pressure lava crystallisation. The lowest Al^{iv} in our experiments occurs in dry and damp experiments at low temperature where orthopyroxene coexists with plagioclase. Consequently, Al^{iv} is an indicator of phenocryst crystallization from differentiated, plagioclase-bearing melts.

Amphibole

Amphibole phenocrysts are lacking in St Vincent lavas but prevalent in xenoliths and in our experiments. Experimental amphiboles have high Mg# compared to xenolith amphiboles (Fig. 15d). A single amphibole from damp experiment BM52 (1 GPa, 1000 °C) overlaps the high Al^{iv}-Mg# end of the xenolith array. Two experiments (BM60 and 1-9 of Pichavant & Macdonald, 2007) show anomalously low Al^{iv}, well below any natural amphiboles (Fig. 15d).

Plagioclase

The compositional range of plagioclase in lavas is An_{90} to An_{36} (Heath et al., 1998a, Robertson, 2002), whereas plagioclase in xenoliths is homogeneous and anorthitic (An_{97} to An_{82}), The one of most striking features of St Vincent cumulates is coexistence of An-rich plagioclase with relatively evolved olivine (Fo_{67-80}; grey bars in Fig. 16). Experimental olivine-plagioclase pairs only attain such characteristics at relatively low pressures (0.4 GPa), temperatures (≤ 1050 °C) and water-saturated conditions (Fig. 16). At other conditions experimental plagioclase is more sodic (An_{47-77}) and olivine is more magnesian (Fo_{93-85}) than in plutonic xenoliths. Low Fo olivines co-precipitating with An-rich plagioclase appears to require crystallisation of H_2O-rich melts that have undergone significant prior differentiation (Tollan et al., 2012).

DISCUSSION

Integration of our experimental results with natural data for lavas and plutonic xenoliths allows us to draw inferences about conditions of magmatic differentiation beneath St. Vincent. In drawing these inferences we make a distinction between liquid compositions, as represented by experimental glasses and lavas, residual minerals, such as those produced in experiments, and phenocrysts, formed during cooling and degassing of lavas prior to eruption. The plutonic xenoliths may represent either residual mineral assemblages or aggregations of phenocrysts.

For the wet series of experiments we have determined a possible condition of equilibrium with lherzolitic mantle at 1.3 GPa and 1180 °C, in agreement with Pichavant et al. (2002). No such condition was identified for the damp series. Pichavant et al. (2002) suggest that lower H_2O magmas equilibrated with lherzolite at lower pressures and higher temperatures. It is not possible to confirm or refute this proposal based on our experiments alone, although extrapolation of the 1.3 GPa damp phase relations suggests that lherzolite equilibrium will occur at slightly higher P and T than for wet basalts. For the purposes of this discussion we

consider that parental HMB with ~4.5 wt% H_2O last equilibrated with peridotite mantle wedge at ~1180 °C and 1.3 GPa. Slightly wetter and drier HMB may also have been generated in the mantle wedge and variability in primary magma H_2O contents is consistent with the melt inclusion study of Bouvier et al (2008).

Polybaric crystallization beneath St Vincent

Lava compositions on St. Vincent are reproduced well by our experiments, suggesting that lower crustal differentiation of mantle-derived HMB is capable of generating the observed diversity of erupted magmas (Fig. 12). In Table 4 we compare the average compositions of natural lavas with experimental glasses to explore the range of natural differentiation conditions that can produce the principal lava varieties. We calculate the mean and standard deviation for each of the lava varieties from the number of analyses denoted *n* in Table 4. Comparison to the experimental glasses reveals that discrete *P-T*-H_2O conditions give rise to melts whose compositions correspond to these different varieties (Table 4).

On Figure 17 we present a cartoon showing the generation of different types of lava in St Vincent by polybaric crystallization of mantle-derived HMB parents. HMB themselves are generated within the mantle wedge by hydrous melting of peridotite. The P-T positions of last equilibration of HMB with peridotite (stars in Fig. 17) lie slightly above the mantle wedge geotherm of Syracuse et al. (2010) presumably because of heat advection by ascending magma. HMB slightly more evolved than our starting composition can be generated by modest olivine or pyroxene crystallization within the mantle wedge (≥1.3 GPa). LMB are generated by crystallisation of wet or damp basalts at pressures of 1.0 to 1.3 GPa. Residua are wehrlite or websterite. Wet and damp basalts are unable to generate LMBs at lower pressure conditions. BA are generated by differentiation of dry or damp HMB at slightly lower pressures (0.7-1.0 GPa). Residua are hornblende websterite (damp) or gabbronorite (dry).

These findings are consistent with a magma differentiation region straddling the Moho fuelled by intrusion of mantle-derived HMB with H_2O contents in the range 2-5 wt%.

Andesites (and plausibly some BA) can also be generated in the lower crust but from dry HMB ($H_2O \approx 0.6$ wt%). In an arc setting this is somewhat counter-intuitive, especially as melt inclusion studies (Bouvier et al. 2008) that show no evidence for such dry parental magmas on St. Vincent. It is striking that 0.6 wt% H_2O is approximately that which can be structurally bound in gabbros with ~30% amphibole. Thus andesites (and some BA) appear to reflect not crystallization of relatively dry basalts, but partial remelting of gabbros formed by the solidification of ancestral HMB. This is consistent with the hot-zone concept of Annen et al. (2006) in which derivative melts are generated by a combination of crystallization and partial melting of the lower crust. In the case of St. Vincent, where isotopic data (Heath et al., 1998b) testify to negligible old crust in magma generation, the lower crust is likely composed almost exclusively of partially solidified hydrous basalts (hornblende gabbros). As the hot zone matures thermally these older gabbros will be heated sufficiently to partially melt, generating andesites and some BA. Unfortunately, our dry experiments were performed only at 1.0 GPa and we cannot exclude the possibility of andesite generation at other pressures. Nonetheless, generation of andesites at around 30 km depth by partial melting of hornblende gabbros of HMB composition is in keeping with studies of other arcs where more evolved magmas are thought to be produced by remelting of ancestral solifidied magma, e.g. generation of Izu-Bonin rhyolites from solid andesites (Tamura & Tatsumi 2002). The time taken to generate sufficiently high hot-zone temperatures for andesite generation beneath St. Vincent by remelting gabbros will depend on HMB input rates into the lower crust. In the hot zone simulations presented by Melekhova et al (2013) temperatures over 1050 °C are generated in a region 1.2-1.3 km thick above the region of basalt generation (30 km depth) after 2 Ma (10 mm yr^{-1} injection rate) or 0.9 Ma (20 mm yr^{-1}), timescales entirely commensurate with the

volcanic history of St. Vincent. Radiometric dating of different St. Vincent lava types is required to test the hypothesis that andesite eruption post-dates the first evidence of HMB magmatism by approximately 1 Ma. The concurrent generation of BA, LMB and andesites at similar lower crustal depths by both crystallization and partial melting is likely to lead to extensive mixing between these different magma types (e.g. Annen et al., 2006; Melekhova et al., 2013).

The origin of HAB (SiO_2 48-53 wt%, Al_2O_3 > 20 wt%, CaO > 8.5 wt%, MgO < 9 wt%) in arcs has been the subject of longstanding debate (e.g. Marsh, 1976; Myers, 1988; Brophy, 1989; Bartels et al., 1991; Kersting & Arculus, 1994; Ozerov, 2000). The experiments presented here and those of Pichavant & Macdonald (2007) indicate that HAB are products of clinopyroxene-rich crystallisation of HMB with high initial H_2O content (≥4 wt%) at mid to upper crustal conditions, 0.4 GPa, and temperatures of 1050-1080°C (e.g. Crawford et al., 1987; Draper & Johnston, 1992, Sisson and Grove 1993b; Grove et al., 2003, Chiaradia et al., 2011).

Our proposal of polybaric differentiation of HMB with variable, but elevated, H_2O contents beneath St. Vincent is consistent with several independent lines of evidence. The most direct evidence for elevated H_2O contents comes from analyses of melt inclusions (Bouvier et al., 2008), which lie in the range 0.8 to 5.2 wt%. The highest value corresponds to a saturation pressure of about 0.24 GPa, assuming that there is no dissolved CO_2, providing a minimum pressure estimate for trapping. Heath et al. (1998a) report melt inclusion analyses from a variety of host minerals. They do not report H_2O directly, but estimates using the by-difference method yield values up to 9.4 wt% in dacitic melt inclusions. Notwithstanding the relative imprecision of this method, the inferred minimum pressure of trapping is around 0.4 GPa.

It has been proposed (Davidson et al, 2007) that many arc magma suites show evidence of amphibole fractionation in their differentiation, despite the relative scarcity of amphibole as a phenocryst phase. This idea gives rise to the notion of "cryptic" amphibole fractionation. Our experiments lend support to this idea. The prevalence of amphibole in plutonic xenoliths also testifies to crystallization of some magmas at depths where amphibole is stable. Amphibole stability is sensitive to a number of factors, including pressure, H_2O and bulk composition. There is considerable experimental evidence that amphibole can crystallize from basalts, andesites and dacites at pressures as low as 0.15 GPa (e.g. Allan & Boettcher, 1978; Geschwind & Rutherford, 1992; Barclay & Carmichael, 2004). However, amphibole saturation occurs at relatively low temperatures and has a correspondingly low Mg#. To generate amphiboles with Mg# ≈ 0.72, as observed in some St. Vincent xenoliths (Fig. 15d), requires early amphibole crystallization from magnesian basalt melts. In our experiments amphibole saturation from such melts is limited to pressures ≥ 0.7 GPa.

Polybaric crystallization can also account for CaO-MgO systematics in St. Vincent lavas that show a wide range of CaO at any given MgO content (Fig.12g and Fig.18). This variability arises because at lower pressure clinopyroxene appears at increasingly lower temperatures than olivine, leading to elevated CaO in derivative melts. Our experimental glasses show that with decreasing pressure (isobars shown on Fig.18) there is a systematic increase in CaO, with the highest CaO melts occurring at 0.4 GPa. Our experimental results together with Pichavant & Macdonald (2007) show that high CaO (>10 wt%), low MgO (<8 wt%) lavas can be produced from HMB parents only at pressures < 0.7 GPa (Fig. 18). It should be noted, however, that the systematic increase of CaO with decreasing pressure is only true for melts with CaO contents above 9.4 wt% (Fig.18, dashed line). Below this value melt composition is influenced strongly by amphibole and plagioclase crystallisation.

Cumulate compositions further support polybaric crystallization of St Vincent magmas at elevated H_2O contents. Most of our experiments failed to reproduce crystal compositions in the plutonic xenoliths or lava phenocrysts suggesting that the phenocrysts and xenoliths do not represent fragments of the residual cumulate assemblage from the deep crustal differentiation region, but instead correspond to lower-pressure crystallization from evolved melts. Crystallization in these hydrous derivative melts may be initiated at depths where they intersect their H_2O-saturated liquidus (Annen et al, 2006). Adiabatic ascent may explain the agreement between magma generation temperatures from our experiments and eruption temperatures from mineral thermometry (Heath et al., 1998a; Robertson, 2002). Therefore, the mineral assemblages and compositions of plutonic xenoliths are ascribed to shallow-level crystallization of evolved melts that were themselves generated by differentiation of HMB at higher pressures. A good example are troctolites, which have been shown to require H_2O rich, low-MgO ($\leq$ 6wt%) melt with high-Al_2O_3 ($\geq$ 19 wt%) content (HAB) crystallised at $\leq$ 0.4 GPa. This proposal is in agreement with Plechov et al. (2008) who suggest that allivalite xenoliths ($Fo_{<81}$, $An_{>90}$) from the Kuril-Kamchatka arc, Russia, are products of high-Al basalts (4-7 wt% MgO and 17-19 wt% Al_2O_3) that are themselves differentiation products of primitive HMB with 3-3.5 wt% H_2O, crystallised at 970-1080 °C and ~0.1 GPa.

Deep versus Shallow Differentiation

Our experimental results support the generation of diverse arc magmas by differentiation of mantle-derived HMB over a range of near-Moho and lower crustal pressures. This is in contrast to other models of arc magma differentiation that focus instead on crystallization in the mid or shallow crust. One such example is the Cascades arc where Blatter et al. (2013) use experimental evidence to rule out deep crustal differentiation to generate the erupted magma types. To explore whether deep crustal differentiation is also possible in the Cascades we have combined our experimental results with studies by Pichavant et al. (2007) and Sisson et

al. (2005). All three studies involve basalts with comparable initial water content, although those of Sisson et al. (2005) are slightly more evolved (4-5 wt% MgO; 18-20 wt%Al_2O_3), so more akin to LMB than HMB. The experimental glasses are compared to a compilation of data from the Cascades (using the GEOROC database - http://georoc.mpch-mainz.gwdg.de/georoc) and St. Vincent (Heath et al., 1998a and Robertson, 2002) in terms of aluminum saturation index (ASI) vs SiO_2 wt% (Fig.19). The domains of experimental crystal composition for plagioclase, amphibole and clinopyroxenes are shown by ellipses and from St. Vincent cumulate xenoliths by triangles. The two coloured fields demonstrate the composition of lavas produced dominantly by crystallization of amphibole or plagioclase, or by the combination of both, where colours overlap. The dashed lines with arrows are isobars for damp and wet experiments, blue and red respectively, from this study and from Pichavant and Macdonald (2007), black. The mineral domains illustrate very well the trajectory of melt evolution. Extended clinopyroxene crystallization leads to a very steep increase in ASI; amphibole also increases ASI, but to lesser extent because of its lower SiO_2 content; plagioclase crystallisation limits ASI increase. As plagioclase crystallization is suppressed by the presence of H_2O, damp and wet experiments show a steady increase in ASI at high temperatures (low SiO_2) independent of pressure, until amphibole become stable. This is in marked contrast to dry experiments, where plagioclase stability extends to high temperatures and ASI increase is muted.

The 0.7 GPa experimental data of Sisson et al. (2005) illustrate the effect of starting composition on melt evolution. Their low-Mg, high-Al starting composition is shown on Figure 19 by a purple star. Their experimental products are dominantly plagioclase + amphibole, with plagioclase proportion increasing at lower temperatures, in very good agreement with our observations. It is apparent from Fig. 19 that generation of evolved Cascades lavas does not require low-pressure differentiation, unless the starting point for that

differentiation is a basalt whose ASI has already been elevated by prior crystallization of hydrous HMB at elevated pressure. In that case, further limiting ASI increase can only be effected by shallow, plagioclase-dominated crystallization, as proposed by Blatter et al (2013). If differentiation of HMB with 2.3 wt% H_2O occurs at pressures 0.7-1.3 GPa then extreme enrichment in ASI does not occur. We conclude that the array of Cascades composition could be produced by polybaric, lower to mid crustal differentiation of HMB with variable initial water content, in a fashion similar to St Vincent. However we do not exclude the possibility of magma mixing and assimilation of older crustal materials.

CONCLUSIONS

Our experimental results show that St. Vincent magmas and plutonic xenolith could be generated by polybaric fractionation of mantle-derived HMB with variable, but elevated H_2O content. Other key findings include:

1. Melt Fraction - temperature relationships are non-linear and a consequence of the changing crystallising assemblages. Rapid change in melt fraction occurs during eutectic-like behavior, i.e. melt and crystalline residue have similar composition, when rapid change in melt composition appears during peritectic-like behavior.

2. A distinction should be drawn between those mineral phases that are residual during deep crustal differentiation and those that occur as phenocrysts in lavas. The latter are interpreted as the products of relatively shallow crystallization, plausibly as ascending hydrous magmas attain their H_2O-saturated liquidi in the shallow crust. The disconnect between residual and phenocryst minerals may give rise to cryptic fractionation (e.g. Davidson et al 2007), especially if the residual assemblage contains amphibole which is lacking in lavas.

3. Cumulate assemblages are very sensitive to pressure, temperature and H_2O content of parental melt. Cumulate xenoliths of St. Vincent are produced by relatively shallow

crystallization of variously differentiated magmas rather than as residual assemblages from the deep crustal source regions of such magmas. Amphibole-bearing gabbroic and wehrlitic cumulate xenoliths were crystallised from melts of basaltic andesite and andesitic compositions at temperatures below 1110 °C and near H_2O-saturated conditions. Troctolite cumulates characterized by coexistence of high-An plagioclase with low-Fo olivine form from low-pressure crystallization of HAB melt.

4. Andesites on St Vincent most likely are products of partial remelting of precursor HMB that had solidified at depth to produce gabbros with ~30% hornblende, i.e. ~0.6 wt% structurally-bound H_2O.

REFERENCES

Adam, J. & Green, T. H. (1994). The effects of pressure and temperature on the partitioning of Ti, Sr and REE between amphibole, clinopyroxene and basanitic melts. *Chemical Geology* **117**, 219-233.

Allen, J. C. & Boettcher, A. L. (1978). Amphiboles in the andesite and basalt: II. Stability as a

function of P-T-fH$_2$O-fO$_2$. *American Mineralogist* **63**, 1074-1087.

Alonso-Perez, R., Muntener, O. & Ulmer, P. (2009). Igneous garnet and amphibole

fractionation in the roots of island arcs: experimental constraints on andesitic liquids

Contributions to Mineralogy and Petrology **157**, 541-558.

Annen, C., Blundy, J. D. & Sparks, R. S. J. (2006). The Genesis of Intermediate and Silicic Magmas

in Deep Crustal Hot Zones. *Journal of Petrology* **47**, 505-539.

Arculus, R. J. (1976). Geology and geochemistry of the alkali basalt-andesite association of

Grenada, Lesser Anrilles island arc. *Geological Society of America Bulletin* **87**, 612-624.

Arculus, R. J. (1978). Mineralogy and petrology of Grenada, Lesser Antilles Island Arc.

Contributions to Mineralogy and Petrology **65**, 413-424.

Arculus, R. J. & Wills, K. J. A. (1980). The petrology of plutonic blocks and inclusions from

the Lesser Antilles Island Arc. *Journal of Petrology* **21**, 743-799.

Ballhaus, C., Berry, R. F. & Green, D. H. (1991). High pressure experimental calibration of

the olivine-orthopyroxene-spinel oxygen geobarometer: implications for the oxidation state of

the upper mantle. *Contributions to Mineralogy and Petrology* **107**, 27-40.

Barclay, J. & Carmichaael, I. S. E. (2004). A Hornblende Basalt from Western Mexico:

Water-saturated Phase Relations Constrain a Pressure-Temperature Window of Eruptibility.

Journal of Petrology **45**, 485-506.

Barnes, S. J. & Roeder, P.L. (2001). The Range of spinel compositions in Terrestrial Mafic and

Ultramafic Rocks. Journal of Petrology 42, 2279-2302.

Bartels, K. S., Kinzler, R. J. & Grove, T. L. (1991). High pressure phase relations of primitive high-

alumina basalts from Medicine Lake volcano, northern California. *Contributions to Mineralogy and*

Petrology **108**, 253-270.

Berry, A. J., O'Neill, H. S. C., Jayasuriya, K. D., Campbell, S. J. & Foran, G. J. (2003).

XANES calibrations for the oxidation state of iron in a silicate glass. *American Mineralogist*

88, 967-977.

Blatter, D. L., Sisson, T. W. & B. Hankins, W. (2013). Crystallization of oxidized, moderately hydrous arc basalt at mid- to lower-crustal pressures: implications for andesite genesis. *Contributions to Mineralogy and Petrology* **166**, 861-886.

Brooker, R., Holloway, J. R. & R.Hervig. (1998). Reduction in piston-cylinder experiments: The detection of carbon infiltration intoplatinum capsules. *American Mineralogist* **83**, 985-994.

Botcharnikov, R. E., Koepke, J., Holtz, F., McCammon, C. & Wilke, M. (2005). The effect of water activity on the oxidation and structural state of Fe in a ferro-basaltic melt. *Geochimica et Cosmochimica Acta* **69**, 5071-5085.

Briden, J. C., Rex, D. C., Faller, A. M. & Tomblin, J. F. (1979). K-Ar gechronology and palaeomagnetism of volcanic rocks in the Lesser Antilles island arc. *Philosophical Transactions of the Royal Society of London* **A291**, 485-528.

Bouvier, A. S., Metrich, N. & Deloule, E. (2008). Slab-Derived Fluids in the Magma Sources of St.Vincent (Lesser Antilles Arc): volatile and light element Imprints. *Journal of Petrology* **49**, 1427-1448.

Brophy, J. G. (1989). Basalt convection and plagioclase retention: model for the generation of high-alumina arc basalt. *Geology* **97**, 319-329.

Brown, G. M., Halland, J. G., Sigurdsson, H., Tomblin, J. F. & Arculus, R. J. (1977). Geochemistry of Lesser Antilles volcanic island arc. *Geochimica et Cosmochimica Acta* **41**, 785-801.

Burnham, C. W. (1979). The importance of volatile constituents. In: Yoder, H. S. (ed.) *The Evolution of Igneous Rocks*: Princeton University Press, **439-482**.

Chiaradia, M., Muntener, O. & Beate, B. (2011). Enriched Basaltic Andesites from Mid-crustal Fractional Crystallization, Recharge, and Assimilation (PilavoVolcano, Western Cordillera of

Ecuador). *Journal of Petrology* 52, 1107-1147.

Christeson, G.L., Mann, P., Escalona, A. & Aitken, T.J. (2008). Crustal structure of Caribbean-northeastern South America arc-continent collision zone. Journal of Geophysical Research, 113, B08104.

Cottrell, E., Kelley, K. A., Lanzirotti, A. & Fischer, R. A. (2009). High-precision determination of iron oxidation state in silicate glasses using XANES. *Chemical Geology* **268**, 167-179.

Crawford, A. J., Falloom, T. J. & Eggins, S. (1987). The origin of island arc high-alumina basalts. *Contributions to Mineralogy and Petrology* **97**, 417-430.

Davidson, J., Turner, S., Handley, H., Macpherson, C. & Dosseto, A. (2007). Amphibole "sponge" in arc crust? *Geology* **35**, 787-790.

Di Carlo, I. D., Pichavant, M., Rotolo, S. G. & Scaillet, B. (2006). Experimental crystallization of a high-K arc basalt: the Golden Pumice, Stromboli Volcano (Italy). *Journal of Petrology* **47**, 1317-1343.

Draper, D. S. & Johnston, A. D. (1992). Anhydrous PT phase relations of an Aleutian high-MgO basalt: an investigation of the role of olivine-liquid reaction in the generation of arc high-alumina basalts. *Contributions to Mineralogy and Petrology* **112**, 501-519.

Eggins, S. M. (1993). Origin and differentiation of picritic arc magmas, Ambae (Aoba), Vanuatu. *Contributions to Mineralogy and Petrology* **114**, 79-100.

Farges, F., Rossano, S., Lefrere, Y., Wilke, M. & Jr., G. B. (2005). Iron in silicate glasses: a systematic analysis of pre-edge, XANES and EXAFS features. *Physica Scripta* **T115**, 957.

Gaetani, G. A., Grove, T. L. & Bryan, W. B. (1993). The influence of water on the petrogenesis of subduction-related igneous rocks. *Nature* **365**, 332-334.

Gaetani, G. A. & Grove, T. L. (1998). The influence of water on melting of mantle peridotite. *Contributions to Mineralogy and Petrology* **131**, 323-346.

Geothermica Italiana, srl. (1992). Exploration for geothermal resources in the Eastern Caribbean. *Island Report: St. Vincent. Pisa: United Nations – DTCD, CARICOM – Secretariat.*

Geschwind, C.-H. & Rutherford, M. J. (1992). Cummingtonite and the evolution of the Mount St. Helens (Washington) magma system: Am experimental study. *Geology* **20**, 1011-1014.

Grove, T. L., Donnelly-Nolan, J. M. & Housh, T. (1997). Magmatic processes that generated the rhyolite of Glass Mountain, Medicine Lake volcano, N. California. *Contributions to Mineralogy and Petrology* **127**, 205-223.

Grove, T. L., Elkins-Tanton, L. T., Parman, S. W., Chatterjee, N., Muntener, O. & Gaetani, G. A. (2003). Fractional crystallization and mantle-melting controls on calc-alkaline differentiation trends. *Contributions to Mineralogy and Petrology* **145**, 515-533.

 Hall, J. L. (2004). Iron and water losses from hydrous basalts contained in Au80Pd20 capsules at high pressure and temperature. *Mineralogical Magazine* **68**, 75-81.

Hawkesworth, C. J., O'Nions, R. K. & Arculus, R. J. (1979). Nd and Sr isotope geochemistry of island arc volcanics, Grenada, Lesser Antilles. *Earth and Planetary Science Letters* **45**, 237-248.

Heath, E., Macdonald, R., Belkin, H., Hawkesworth, C. & Sigurdsson, H. (1998a). Magmagenesis at Soufriere Volcano, St Vincent, Lesser Antilles Arc. *Journal of Petrology* **39**, 1721-1764.

Heath, E., Turner, S. P., Macdonald, R., Hawkesworth, C. J. & Casteren, P. v. (1998). Long magma residence times at an island arc volcano (soufriere, St Vincent) in the Lesser Antilles: evidence from U-238-Th-230 isochron dating. *Earth and Planetary Science Letters* **160**, 49-63.

Holloway, J. R. & Burnham, C. W. (1972). Melting relations of basalt with equilibrium water pressure less than total pressure. *Journal of Petrology* **13**, 1-29.

Johannes, W. & Holtz, F. (1996). Petrogenesis and Experimental Petrology of Granitic Rocks.

Minerals and Rocks. Berlin: Springer-Verlag, **20**.

Kägi, R., Muntener, O., Ulmer, P. & Ottolini, L. (2005). Piston-cylinder experiments on H_2O undersaturated Fe-bearing systems: An experimental setup approaching $f(O_2)$ conditions of natural calc-alkaline magmas. *American Mineralogist* **90**, 708-717.

Kelley, K. A., Plank, T., Newman, S., Stolper, E. M. & Grove, T. L. (2010). Mantle melting as a function of water content beneath the Mariana Arc. *Journal of Petrology* **51**, 1711-1738.

Kersting, A. B. & Arculus, R. J. (1994). Klyuchevskoy Volcano, Kamchatka, Russia: The role of high-flux recharged, tapped, and fractionated magma chamber(s) in the genesis of high-Al_2O_3 from high-MgO basalts. *Journal of Petrology* **35**, 1-41.

Kopp, H., Weinzierl, W., Becel, A., Charvis, P., Evain, M., Flueh, E. R., Gailler, A., Galve, A., Hirn, A., Kandilarov., A., Klaeschen, D., Laigle, M., Papenberg, C., Planert, L., Roux, E. and Trail and Thales teams. (2011). Deep structure of the central Lesser Antilles Island Arc: Relevance for the formation of continental crust. Earth and Planetary Science Letters, 304, 121-134.

Kress, V. C. & Carmichael, I. S. E. (1991). The comprossibility of silicate liquids containing Fe2O3 and the effect of composition, temperature, oxygen fugacity and pressure on their redox states. *Contributions to Mineralogy and petrology* **108**, 82-92.

Leake, B. E., Woolley, A. R., Arps, C. E. S., Birch, W. D., Gilbert, M. C., Grice, J. D., Hawthorne, F. C., Kato, A., Kisch, H. J., Krivovichev, V. G., Linthout, K., Laird, J., Mandarino, J. A., Maresch, W. V., Nickel, E. H., Rock, N. M. S., Shumacher, J. C., Smith, D. C., Stephrnson, N. C. N., Ungaretti, L., Whittaker, E. J. W. & Youzhi, G. (1997). Nomenclature of amphiboles: report of the subcommittee on amphiboles of the international mineralogical association, commission on new minerals and mineral names. *The Canadian Mineralogist* **35**, 219-246.

Lesne, P., Kohn, S. C., Blundy, J., Witham, F., Botcharnicov, R. E. & Behrens, H. (2011).

Experimental simulation of closed-system degassing in the System Basalt-H_2O-CO_2-S-Cl. *Journal of Petrology* **52**, 1737-1762.

Lewis, J. F. (1973a). Petrology of ejected plutonic blocks of Soufriere volcano, St Vincent, West-Indies. *Journal of Petrology* **14**, 81-&.

Lewis, J. F. (1973b). Mineralogy of the ejected plutonic blocks of the Soufriere volcano St. Vincent: olivine, pyroxene, amphibole and Magnetite paragenesis. *Contributions to Mineralogy and Petrology* **38**, 197-220.

Macdonald, K. C. & Holcombe, T. L. (1978). Investigation of magnetic anomalies and sea floor spreding in the Cayman Trough. *Earth and Planetary Science Letters* 40, 407-414.

Marsh, B.D. On the crystallinity, probability of occurrence, and rheology of lava and magma. *Contributions to Mineralogy and Petrology* **78**, 85-98 (1981).

Macdonald, R., Hawkeswoorth, C. J. & Heath, E. (2000). The Lesser Antilles volcanic chain: a study in arc magmatism. *Earth-Science Reviews* **49**, 1-76.

Matzen, A. K., Baker, M. B., Beckett, J. R. & Stolper, E. M. (2011). Fe-Mg partitioning between olivine and high-magnesian melts and the nature of Hawaiian parental liquids. *Journal of Petrology* **52**, 1243-1263.

McDade, P., Wood, B. J., Westrenen, W. V., Brooker, R., Gudmundsson, G. & Soulard, H. (2002). Pressure corrections for a selection of piston-cylinder cell assemblies. *Mineralogical Magazine* **66**, 1021-1028.

Médard, E. & Grove, T. L. (2008). The effect of H_2O on the olivine liquidus of basaltic melts: experiments and thermodynamic models. *Contributions to Mineralogy and Petrology* **155**, 417-432.

Melekhova, E., Annen, C. & Blundy, J. (2013). Compositional gaps in igneous rock suites controlled by magma system heat and water content. *Nature Geoscience* **6**, 385-390.

Miyashiro, A. (1974). Volcanic rock series in island arcs and active continental margins.

American Journal of Science 275, 321-355.

Müntener, O., Kelemen, P. B. & Grove, T. L. (2001). The role of H2O during crystallization of primitive arc magmas under uppermost mantle conditions and genesis of igneous pyroxenites: an experimental study. *Contributions to Mineralogy and Petrology* **141**, 643-658.

Myers, J. D. (1988). Possible petrogenetic relations between low- and high-MgO Aleutian basalts. *Geological Society of America Bulletin* **100**, 1040-1053.

O'Neill, H. S. C. & Wall, V. J. (1987). The olivine-orthopyroxene-spinel oxygen geobarometer, the nickel precipitation curve, and the oxygen fugacity of the Earth's upper mantle. *Journal of Petrology* **28**, 1169-1191.

Ozerov, A. Y. (2000). The evolution of high-alumina basalts of the Kluchevskoy volcano, Kamchatka, Russia, based on microprobe analyses of mineral inclusions. *Journal of Volcanology and Geothermal Research* **95**, 65-79.

Parkinson, I. J., Arculus, R. J. & Eggins, S. M. (2003). Peridotite xenolith from Grenada, Lesser Antilles Island Arc. Contribution to Mineralogy and Petrology 146, 241-262.

Pichavant, M., Mysen, B. O. & Macdonald, R. (2002). Source and H_2O content of high-MgO magmas in island arc settings: An experimental study of a primitive calc-alkaline basalt from St. Vincent, Lesser Antilles arc. *Geochimica et Cosmochimica Acta* **66**, 2193–2209.

Pichavant, M. & Macdonald, R. (2007). Crystallization of primitive basaltic magmas at crustal pressuresand genesis of the calc-alkaline igneous suite: experimental evidence from St Vincent, Lesser Antilles arc. *Contributions to Mineralogy and Petrology* **154**, 535-558.

Plechov, P. Y., Shishkina, T. A., Ermakov, V. A. & Portnyagin, M. V. (2008). Formation conditions of allivalites, olivine–anorthite crystal enclaves, in the volcanics of the Kuril–Kamchatka Arc. *Petrology* **16**, 232-260.

Portnyagin, M., Bindeman, I., Hoernle, K. & Hauff, F. (2007). Geochemistry of Primitive

Lavas of the Central Kamchatka Depression: Magma Generation at the Edge of the Pacific Plate. In: Eichelberger, J., Gordeev, E., Izbekov, P., Kasahara, M. & Lees, J. (eds.) *Volcanism and Subduction: The Kamchatka Region*: Geophysical Monograph Series, **199-239**.

Pownceby, M. I. & O'Neill, H. S. (1994). Thermodynamic data from redox reactions at high-temperatures. 3. Activity-composition relations in Ni-Pd alloys from EMF-measurements at 850-1250-K, and calibration of the NiO+Ni-Pd assemblage as a redox sensor. *Contributions to Mineralogy and Petrology* **116**, 327-339.

Robertson, R. E. A. (2002). The Volcanic Geology of the Pre-Soufriere rocks on St Vincent, West Indies.: PhD thesis, University of the West Indies.

Roeder, P. L. & Emslie, R. F. (1970). Olivine-Liquid Equilibrium. *Contributions to Mineralogy and Petrology* **29**, 275-289.

Roeder, P. L. & Reynolds, I. (1991). Crystallization of chromite and chromium solubility in basaltic melts. *Journal of Petrology* **32**, 909-934.

Rowley, K. (1978b). Late Pleistocene pyroclastic deposits of Soufriere Volcano, St Vincent. *W.I. Geological Society of America Bulletin* **89**, 825-835

Schuth, S., Rohrbach, A., Münker, C., Ballhaus, C., Garbe-Schönberg, D. & Qopoto, C. (2004). Geochemical constraints on the petrogenesis of arc picrites and basalts, New Georgia Group, Solomon Islands. *Contributions to Mineralogy and Petrology* **148**, 288-304.

Sisson, T. W. & T.L.Grove. (1993a). Experimental investigations of the role of H20 in calc-alkaline differentiation and subduction zone magmatism. *Contributions to Mineralogy and Petrology* **113**, 143-166.

Sisson, T. W. & Grove, T. L. (1993b). Temperatures and H2O contents of low-MgO high-alumina basalts. *Contributions to Mineralogy and Petrology* **113**, 167-184.

Sisson, T. W., Ratajeski, K., Hankins, W. B. & Glazner, A. F. (2005). Voluminous granitic magmas from common basaltic sources. *Contributions to Mineralogy and Petrology* **148**, 635-661.

Skulski, T., Minarik, W. & Watson, E. B. (1994). High-pressure experimental trace-element partitioning between clinopyroxene and basaltic melts. *Chemical Geology* **117**, 127-147.

Stamper, C. C., Melekhova, E., Blundy, J. D., Arculus, R. J., Humphreys, M. C. S. & Brooker, R. A. (2014). Oxidised phase relations of a primitive basalt from Grenada, Lesser Antilles. *Contributions to Mineralogy and Petrology* **167**:954.

Streckeisen. (1976). To each plutonic rock its proper name. *Earth-Science Reviews*, Amsterdam: Elsevier Scientific Publishing Company, **1-33**.

Syracuse, E. M., Keken, P. E. v. & Abers, G. A. (2010). The global range of subduction zone thermal models. *Physics of the Earth and Planetary Interiors* **183**, 73-90.

Tamura, Y. & Yoshiyuki, T. (2002). Remelting of an Andesitic Crust as a Possible Origin for Rhyolitic Magma in Oceanic Arcs an Example from the Izu-Bonin Arc. Journal of Petrology, 43, 1029-1047.

Tollan, P. M. E., Bindeman, I. & Blundy, J. D. (2012). Cumulate xenoliths from St. Vincent, Lesser Antilles Island Arc: a window into upper crustal differentiation of mantle-derived basalts. *Contributions to Mineralogy and Petrology* **163**, 189-208.

Toothill, J., Williams, C. A., Macdonald, R., Turner, S. P., Rogers, N. W., Hawkesworth, C. J., Jerram, D. A., Ottley, C. J. & Tindle, A. G. (2007). A complex petrogenesis for an arc magmatic suite, St Kitts, Lesser Antilles. *Journal of Petrology* **48**, 3-42.

Toplis, M. J. (2005). The thermodynamics of iron and magnesium partitioning between olivine and liquid: criteria for assessing and predicting equilibrium in natural and experimental systems. *Contributions to Mineralogy and Petrology* **149**, 22-39.

Villiger, S., Ulmer, P., Muntener, O. & Thompson, A. B. (2004). The liquid line of descent of anhydrous, mantle-derived, tholeiitic liquids by fractional and equilibrium crystallization—an experimental study at 1_0 GPa. *Journal of Petrology* **45**, 2369-2388.

Villiger, S., Ulmer, P. & Müntener, O. (2007). Equilibrium and fractional crystallization

experiments at 0.7GPa; the effect of pressure on phase relations and liquid compositions of tholeiitic magmas. *Journal of Petrology* **48**, 159-184.

Wilke, M., Farges, F., Petit, P. E., Brown, G. E. & Martin, F. (2001). Oxidation state and coordination of Fe in minerals: An Fe K-XANES spectroscopic study. *American Mineralogist* **86**, 714-730.

Yamamoto, M. (1988). Picritic primary magma and its source mantle for Oshima-Oshima and back-arc side volcanoes, Northeast Japan arc. *Contributions to Mineralogy and Petrology* **99**, 352-359.

FIGURE CAPTIONS

Figure 1. (a) The Lesser Antilles region showing the location of 19 volcanic centres considered active or potentially active. The islands shown in brown are Volcanic Caribbees, and in yellow are Limestone Caribbees. (b) Geological map of St.Vincent showing the distribution of the main deposits on the island, adapted from Geothermica Italiana (1992). Boundaries between geological regions are approximate. The location of high-Mg basalt starting material RSV49 is shown.

Figure 2. Backscattered SEM images of run products: (a) BM36 showing inner AuPd sample and Pd sensor capsules surrounded by basalt within outer Pt capsule; (b) inner capsule of BM36 showing a homogeneous distribution of phases; (c) inner capsule of BM37 showing concentration of solid phases at base; (d) close up of inner capsule of BM37 showing sector zoning in clinopyroxene.

Figure 3. Oxygen fugacity, expressed in log units relative to NNO, of runs with *0.6*, *2.3* and *4.5* wt% H_2O. Dashed circles – calculated from NiPd sensor (these tend to be underestimates due to exhaustion of H_2O in sensor capsule); diamonds – calculated from algorithm of Kress & Carmichael (1991) with Fe^{3+} analysed by μXANES. Bars on right side show ΔNNO for

experiments of P&M_07 (Pichavant & Macdonald, 2007) and P et al_02 (Pichavant et al, 2002). Estimates, using the olivine-spinel oxybarometer of Ballhaus et al. (1991), of fO_2 for St Vincent lavas. are shown as dashed lines (our calculation using Robertson (2002) data) and grey bar (Heath et al., 1998).

Figure 4. Phase relations for experimental series with 0.6, 2.3 and 4.5 wt% H_2O. Abbreviations as in Table 2, with *L* indicating liquid. The liquidus was bracketed only at 1.3 GPa with 2.3 wt% of H_2O and at 1 GPa with 0.6 wt% of H_2O. Elsewhere the liquidus was estimated (Medard & Grove, 2008) and shown as a dashed line. Hexagon symbols show phase assemblages. Grey hexagons are experiments by Pichavant & Macdonald (2002) and Pichavant et al. (2007) at similar bulk H_2O contents. Fo and An denote forsterite and anorthite numbers in olivine and plagioclase respectively. Coloured fields represent different cumulate residue assemblages labelled following Streckeisen (1976).

Figure 5. Experimental melt fraction (by weight) as a function of temperature. Open symbols denote extrapolated H_2O-saturated granite solidus (Johannes & Holtz, 1996). Numbers show H_2O content in each experimental glass: bold, SIMS; italics, mass balance. Vertical or near-vertical lines show change in crystallisation sequences as labelled. Abbreviations as in Table 2. Melt fraction uncertainties are smaller than the symbol size in all but one run; temperature uncertainty is ± 10°C.

Figure 6. Composition of experimental spinel presented in terms of Cr# = Cr/(Cr + Al) and Al# = Al/(Al + Cr + Fe^{3+}) plotted against melt fraction (F) (**a, b**) and ΔNNO (**c, d**). Arrows on (**b**) indicate three trends: Al# increasing steadily with decreasing *F*; crystallisation of *pl* (2.3 wt% H_2O) or *hbl+pl* (4.5 wt% H_2O) leading to decreasing Al#. On **c** and **d** spinels are only plotted from our experiments where ΔNNO was calculated from $Fe^{3+}/\Sigma Fe$ (μXANES) and data by P&M, 07 (ΔNNO from sensors). P&M, 07 (Pichavant & Macdonald, 2007); P et al, 02, 1.5/4.5 (Pichavant et al., 2002 experiments with 1.5 and 4.5 wt% H_2O).

Figure 7. Composition of experimental clinopyroxenes (this study, Pichavant & Macdonald, 2007 and Pichavant et al., 2002): **(a)** tschermakite substitution; **(b)** Ca pfu as a function of temperature; **(c)** Ca pfu as a function of pressure; **(d)** Na pfu as a function of pressure.

Figure 8. Composition of experimental amphiboles (symbols as Fig.7): **(a)** Al per formula unit vs Mg# of amphibole, arrow shows drop in Al content of amphibole with progressive plagioclase crystallisation; **(b)** Ti per formula units vs Mg# of amphibole. Dashed lines depict two groups from experiments with 2.3 and 4.5 wt% initial H_2O.

Figure 9. Total alkalis vs silica plot of experimental melts (squares) and St Vincent lavas (circles); data from Heath et al. (1998a) and Robertson (2002).

Figure 10. Compositional variation of experimental melts as a function of temperature for experiments with 0.6, 2.3 and 4.5 wt% H_2O; P&M, 07 (Pichavant & Macdonald, 2007); P et al, 02 (Pichavant et al., 2002). Solid and dashed lines indicate major crystallisation trends showing, where relevant, the controlling influence of melt fraction (*F*), hornblende (*hbl*), magnetite and plagioclase (*pl*). Low temperature, magnetite-saturated melts are labeled in **f**. The arrows in **h** denotes high-CaO and low-CaO trends, labeled *C-series* and *M-series* respectively.

Figure 11. Plot of FeO_{tot}/MgO versus SiO_2 for experimental melts (this study and Pichavant & Macdonald, 2007) and St Vincent lavas (Robertson, 2002 and Heath et al., 1998). The discriminant boundary (dashed line) between tholeiitic and calc-alkaline suits is from Miyashiro (1974). Numbers are fO_2 relative to ΔNNO calculated from $Fe^{3+}/\Sigma Fe$ (μXANES) or sensors (Pichavant & Macdonald, 2007).

Figure 12. Chemical compositions of experimental melts from this study, P&M, 07 - Pichavant & Macdonald (2007) and P et al, 02 – Pichavant et al. (2002) compared to St Vincent lavas (Robertson, 2002; Heath et al, 1998) and melt inclusions (MI - Bouvier et al, 2008; Tollan et al, 2012; Heath et al., 1998). Solid lines show melt evolution in damp

experiments at 0.7 GPa for clarity. Starting materials shown by stars are RSV49 (this study) and STV301 (Pichavant & Macdonald, 2007; Pichavant et al., 2002). Dashed ellipses on **c** and **d** indicate magnetite crystallisation. Note significantly higher CaO concentration in MI from Bouvier et al. (2008). Arrows in **g** show evolution of C-series and M-series (see Fig. 16). The labels H_2O, F (melt fraction), *amphibole* and *pressure* denote the parameters exerting the dominant control on the evolution of different chemical components in the melt.

Figure 13. CaO wt% content of olivine as a function of forsterite (Fo) content. P&M, 07 - Pichavant & Macdonald (2007); P.et al, 02 - Pichavant et al. (2002). Olivine phenocrysts from St. Vincent lavas (Robertson, 2002) are shown with grey symbols: HMB – high magnesium basalt, LMB – low magnesium basalt, BA&A – basaltic-andesite and andesites. MI – hosts to melt inclusions of Bouvier et al. (2008). Cumulate olivines (green triangles) are from Tollan et al. (2012) and Robertson (2002).

Figure 14. Spinel compositions from St Vincent lavas (including starting material RSV49), melt inclusions and cumulates compared to experimental spinels. Legend and data source as in Figures 12 and 13. Labelled arrows in **c** and **d** denote dominant controls on chemical evolution.

Figure 15. Chemical compositions of clinopyroxene **(a)**, orthopyroxene **(b, c)** and amphibole **(d)** from our experiment and experiments by Pichavant & Macdonald (2007) and Pichavant et al. (2002) compared to phenocrysts from St Vincent lavas (Robertson, 2002) and cumulate xenoliths (Robertson, 2002; Tollan et al., 2012, Lewis, 1973a, 1973b). Two dashed circles **(a)** show sector-zoned clinopyroxene from run BM37.

Figure 16. The range of olivine Fo (squares) and plagioclase An (circles) content of experiments as function of temperature. Grey boxes labelled An_{cum} and Fo_{cum} show the range in cumulate compositions and calculated temperatures from Tollan et al. (2012). Filled symbols connected by black lines are coexisting olivine and plagioclase from experiments of

Pichavant & Macdonald (2007), which provide the best match to natural cumulates. The *dry* trend shows decrease of *An* with decreasing temperature in experiments with 0.6 wt% H_2O.

Figure 17. Cartoon of the magma plumbing system beneath St Vincent based on our experimental results. Stars are points of multiple saturation (last equilibration with mantle peridotite), green - this study, black –Pichavant et al., 2002. Labelled fields denote *P-T* regions where experimental glasses match different varieties of lavas (Table 4): HMB – High-MgO basalts, LMB – Low-MgO basalts, HAB - High-Al_2O_3 basalts, BA – basaltic andesites, A – andesites. Colour-coding denotes H_2O content of parent HMB. White arrows show ascent of HMB to P-T regions where differentiated melts are generated. Andesites and some BA appear to be generated by partial remelting of previously solidified gabbros within the lower crust. The wedge geotherm for South Lesser Antilles is from Syracuse et al. (2010); Conrad discontinuity is from Boynton et al. (1979); and Moho is projected from the seismic profiles of Christeson et al. (2008) and Kopp et al (2011).

Figure 18. Plot of CaO versus MgO for experimental glasses (this study –field black symbols; Pichavant & Macdonald (2007) and Pichavant et al. (2002) – empty symbols) and St Vincent natural lavas (Heath et al., 1998; Robertson, 2002) – filled grey circles. Black line shows increasing CaO content generated by olivine-only fractionation. Upon clinopyroxene saturation CaO contents fall along coloured lines denoting approximate isobars. Dashed line shows that in glasses with CaO below 9-9.5 wt% CaO-MgO relation is complicated by crystallisation of plagioclase and amphibole. Experiments labelled *amph-in* demonstrate the effect of sudden abundant crystallisation of amphibole on liquid composition at 1.3 and 1.0 GPa.

Figure 19. Plot of ASI (molar Al/[2Ca+Na+K]) vs wt% SiO_2 for lavas and cumulates from St Vincent (Robertson, 2002 and Heath et al, 1998a) and Cascades arcs (whole rock analyses from GEOROC database) compared to experimental melts from this study, Pichavant &

Macdonald, (2007) and Sisson et al. (2005; S.et al. 05). Labelled ellipses enclose experimental plagioclase, clinopyroxene and amphibole compositions. Triangles are calculated bulk compositions of cumulates. Stars are starting composition from this study and Sisson et al. (2005). Shaded regions show the trajectories of liquid evolution driven by plagioclase + clinopyroxene (yellow) and amphibole (blue) crystallisation. Arrows show isobars (in GPa) for liquid evolution from HMB under wet (red) and damp (blue) conditions. Note that experimental liquids produced from hydrous HMB at pressures of 0.4 to 1.3 GPa are capable of generating the compositional diversity of arc magmas from both St. Vincent and the Cascades.

Table 1. Experimental starting materials

	RSV49[1]	RSV49[2] 2.25 wt% H_2O	RSV49[3] 4.5 wt% H_2O	STV301[4]
SiO_2	47.44	47.67	47.32	47.67
TiO_2	0.75	0.74	0.71	1.09
Al_2O_3	14.48	14.48	14.79	15.50
FeO	8.96	8.93	8.85	8.91
MnO	0.16	0.16	0.16	0.16
MgO	14.56	14.54	14.59	12.68
CaO	10.74	11.00	10.99	11.11
Na_2O	2.28	2.07	2.19	2.26
K_2O	0.24	0.14	0.14	0.48
P_2O_5	0.08	0.09	0.09	0.00
Cr_2O_3	0.26	0.13	0.10	0.11
NiO	0.04	0.05	0.08	0.03
H_2O		2.05	4.5	
mg#	0.743	0.744	0.746	0.717

All analyses calculated 100% anhydrous
[1]St. Vincent basalt from Richardson (2002)
[2]Analysis of glass fused at 1.3 GPa, 1250 °C
[3]Analysis of glass fused at 1.0 GPa, 1200 °C
[4]St Vincent basalt using as starting material by Pichavant et al (2002) and Pichavant et al (2007)

Table 2. Experimental run conditions, phase proportions and assemblages. H$_2$O calc -water in melt from mass balance calculations; * - water saturated run; aH$_2$O - water activity calculated using model of Burnham, 1979; Phase proportions and $\sum$R^2 - from weighted least square calculations; ol -olivine, cpx - clinopyroxene, opx - orthopyroxene, hbl - hornblende, pl - plagioclase, sp - spinel, il - ilmenite, qu - quench; ΔFeO - difference between FeO content in starting material and FeO in the bulk composition as calculated by mass balance calculations in the relative wt%. Positive values are Fe gain, negative Fe loss; H$_2$O SIMS - 4.5/4.36, should be read water in inner capsule/water, in outer capsule.

Run No	Pressure	Temperature	Duration	Phase assemblage and proportions	$\sum$R^2	H$_2$O calc	σ	H$_2$O SIMS	ΔFeO	ΔNNO
	(GPa)	(^{o}C)	(hours)			(wt%)		(wt%)	(%)	sensor
0.6 wt% H$_2$O initial										
RSV49_2	1.0	1350	6	melt(100)				0.6		
RSV49_4	1.0	1270	6	melt(94), ol(5), sp(1)	0.30	0.6	0.01		-10	
RSV49_11	1.0	1250	24	melt(90), ol(5), opx(4), sp(1)	0.04	0.7	0.01			
RSV49_6	1.0	1230	6	melt(23), cpx(37), opx(20), pl(13), sp(7)	0.06	2.6	0.16			
RSV49_7	1.0	1180	24	melt, cpx, opx, pl, sp, il	0.06	na	na			
RSV49_10	1.0	1130	96	melt(19), cpx(38), opx(24), pl(14), sp(5)	0.03	3.2	0.11			
RSV49_9	1.0	1080	96	melt(8), cpx(42), opx(21), pl(20), sp(9)	0.09	7.5	0.9			
RSV49_8	1.0	1030	96	melt(6), cpx(41), opx(24), pl(19), sp(9), il(1)	0.16	10.0	0.98			
2.3 wt% H$_2$O initial										
bmn1	0.4	1080	24	melt(81), ol(17), cpx(1), spl(1), qu	0.27	2.8	0.03			-0.93
BM38	0.7	1200	6	melt(92), ol(7), sp(1), qu	0.12	2.5	0.03	2.50		
BM40	0.7	1150	24	melt(80), ol(13), cpx(6), sp(1)	0.13	2.8	0.04	3.05	-1	
BM43	0.7	1100	24	melt(77), ol(12), cpx(10), sp(1)	0.16	3	0.08	3.02	-1	2.57
BM39	0.7	1050	24	melt(35), cpx(34), opx(15), hbl(11), sp(5)	0.13	5.8	0.3			-0.17
BM58	0.7	1000	27	melt(9), cpx(10), opx(12), hbl(56), pl(11), mag(2)	0.05	13.8	1.2			0.35
BM3	1.0	1200	6	melt(81), ol(12), cpx(4), sp(3), qu	0.30	2.8	0.1	2.94		
BM6	1.0	1100	24	melt(76), ol(10), cpx(10), sp(4)	0.24	3	0.06	4.42		-0.41
BM16	1.0	1080	27	melt(60), cpx(24), opx(14), sp(2), qu	0.28	3.8	0.1	3.88/3.65		0.03

BM41	1.0	1065	23	melt(45), cpx(33), opx(17), sp(5), qu	0.09	5	0.18		-1.5	
BM13	1.0	1050	26	melt(28), cpx(25), opx(12), hbl(34), sp(1), qu	0.11	5.9	0.6			-0.51
BM52	1.0	1000	24	melt(16), cpx(8), opx(7), hbl(69), mag(0.3), qu	0.07	6.3	0.8			0.01
BM60	1.0	950	48	melt(13), cpx(4), opx(4), hbl(76),pl(1), sp(2)	0.01	6.8	1.8			
BM15	1.0	920	26	melt(10), cpx(22), opx(14), hbl(40), pl(11), mag(3)	0.04	15.3*	2.8			0.77
BM45	1.3	1250	6	melt(100)		2.25	0.02	2.05		
BM56	1.3	1150	24	melt(66), cpx(19), opx(13), sp(2), qu	0.04	3.4	0.04			
BM30	1.3	1100	24	melt(52), cpx(30), opx(14), sp(4), qu	0.20	4	0.6		-1	
BM57	1.3	1050	23	melt(34), cpx(37), opx(23), sp(6)	0.28	6.6	0.6		-4	-0.23
4.5 wt% H_2O initial										
bmn2	0.4	1080	24	melt(53), ol(20), cpx(24), sp(3)	0.25	8.3	0.3			0.09
BM33	0.7	1200	6	melt(99), sp(1)	0.20	4.5	0.3	4.46		
BM37	0.7	1150	23	melt(82), ol(13), cpx(3), mag(2)	0.13	5.3	0.1	5.20		
BM34	0.7	1100	27	melt(40), ol(6), cpx(15), hbl(35), mag(4)	0.09	9.7	0.4	7.20		4.98
BM36	0.7	1050	22	melt(34), cpx(8), opx(4), hbl(51), mag(3)	0.19	10.6	0.7	7.90		0.07
BM23	1.0	1200	4	melt(98), sp(2), qu	0.11	4.5	0.01	4.50/4.36		
BM9	1.0	1100	24	melt(79), ol(12), cpx(7), sp(2), qu	0.15	5.7	0.1	5.34	+ 3	0.61
BM17	1.0	1080	24	melt(74), ol(9), cpx(14), sp(3), qu	0.16	6.4	0.15	6.70	+ 2	0.76
BM24	1.0	1030	25	melt(46), ol(7), cpx(13), hbl(33), sp(1), qu	0.06	8.4	0.3	9.30		1.78
BM46	1.3	1250	6	melt(98), sp(2)	0.15	4.6	0.02	4.52		
BM49	1.3	1150	24	melt(62), ol(5), cpx(23), opx(7), sp(3), qu	0.13	7.2	0.3	6.00		
BM32	1.3	1100	24	melt(53), cpx(29), opx(14), sp(4)	0.26	8.7	0.4		-6	
BM50	1.3	1050	26	melt(20), cpx(12), opx(11), hbl(56), mag(1)	0.18	16.6*	2.0			

Table 3. XFe^{3+}** - calculated from Kd = 0.3; ΔNNO* - Kress & Carmichael, 1991; Toplis model - Toplis, 2005; O'Neill & Wall - ol–opx -spinel oxygen geobarometer (1987); values 2.84/4.09 should be read value in inner capsule (in.caps)/value in outer capsule (out.caps).

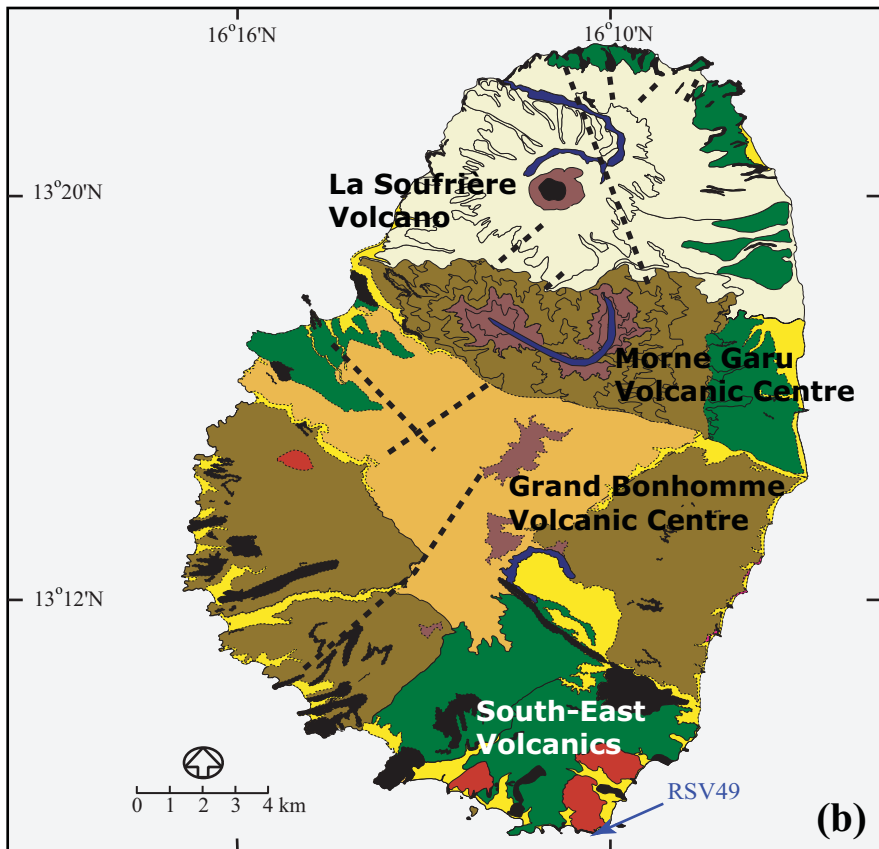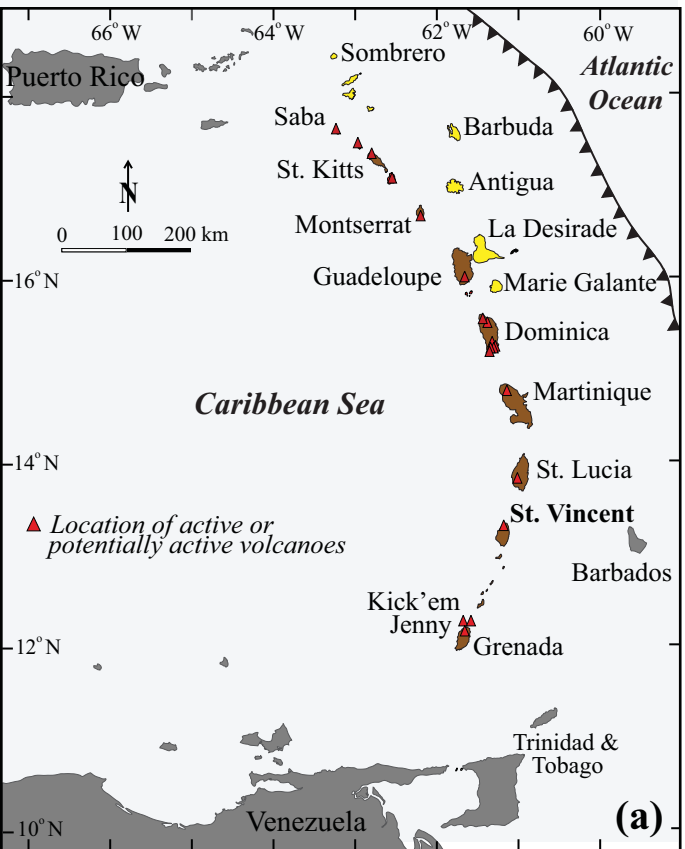| Run No	$Kd_{ol/melt}$ in.caps	$Kd_{ol/melt}$ out.caps	XFe^{3+}**	$Kd_{ol/melt}$ Fe^{2+}	XFe^{3+}	ΔNNO*	XFe^{3+}	σ	$Kd_{ol/melt}$ Fe^{2+}	log fO_2	ΔNNO*	ΔNNO in.caps
	Fe$_{total}$		**Kd of 0.3**	*Toplis model*			*XANES*					*O'Neill & Wall*
0.6 wt% H$_2$O initial												
RSV49_2							0.21	0.01		-4.82	1.4	
RSV49_4	0.29		0.03	0.34	0.15	-2.16	0.28	0.02	0.39	-7.08	-0.24	1.86
RSV49_11	0.18		0.40	0.33	0.45	3.53						2.31
2.3 wt% H$_2$O initial												
bmn1	0.20		0.33	0.39	0.49	3.05						0.87
BM38	0.19		0.36	0.35	0.45	3.22	0.55	0.04		-5.60	2.02	2.24
BM40	0.21		0.31	0.36	0.43	3.02	0.41	0.02	0.35	-5.28	2.92	1.74
BM43	0.17	0.20	0.42	0.35	0.50	3.64						2.48 / 1.70
BM3	0.27		0.11	0.37	0.28	0.33	0.32	0.02	0.39	-5.26	2.32	
BM6	0.32	0.44	-0.07	0.36	0.10	-0.76	0.38/0.52	0.03	0.52	-5.96	2.84/4.09	-0.44
4.5 wt% H$_2$O initial												
bmn2	0.15		0.50	0.45	0.67	5.00						0.08
BM33							0.45	0.03		-6.53	1.21	
BM37	0.12		0.60	0.35	0.66	5.07	0.57	0.04	0.28	-3.98	4.22	4.03
BM34	0.12	0.22	0.60	0.46	0.74	6.05	0.63/0.65	0.04	0.32	-3.91	4.90/5.05	3.88
BM9	0.25	0.32	0.17	0.35	0.29	2.00	0.43	0.03	0.43	-5.55	3.21	0.63 / -0.74
BM17	0.15	0.15	0.50	0.36	0.58	4.59	0.57	0.04	0.34	-4.58	4.44	3.35 / 3.45
BM24	0.22	0.22	0.27	0.38	0.42	3.28						1.8
BM46							0.47	0.03		-5.24	1.96	
BM49	0.15		0.50	0.37	0.59	7.84						3.01

Table 4. Major element composition of representative lavas and matching experimental glasses. Agreement between natural lavas and experimental glasses within 2 σ; * from Robertson (2002).

Sample no.	HMB n=11	st.d	P et a.l #12	P et al. #19	HAB n=13	st.d	bmn2	P&M 4-3	P&M 4-2
SiO_2	**48.02**	**1.17**	48.52	48.19	**50.86**	**1.03**	53.14	51.90	50.20
$Al2O_3$	**15.65**	**0.78**	15.96	15.41	**21.08**	**0.82**	21.45	21.00	20.70
FeO	**9.14**	**0.52**	8.66	8.62	**8.62**	**0.45**	6.98	7.85	8.14
CaO	**10.64**	**0.36**	11.20	11.20	**10.37**	**0.55**	10.51	9.11	10.50
MgO	**12.85**	**1.77**	11.60	12.28	**4.13**	**0.93**	3.47	3.86	5.19
MnO	**0.17**	**0.01**	0.12	0.18	**0.17**	**0.01**	0.15	0.16	0.15
Na_2O	**2.24**	**0.26**	2.27	2.33	**3.29**	**0.38**	2.83	3.76	3.00
K_2O	**0.30**	**0.14**	0.51	0.51	**0.38**	**0.07**	0.24	0.85	0.67
TiO_2	**0.90**	**0.13**	1.13	1.15	**0.98**	**0.09**	1.06	1.51	1.41
$P2O_5$	**0.09**	**0.03**			**0.12**	**0.02**	0.13		
mg#	**0.71**	**0.03**	0.70	0.72	**0.46**	**0.05**	0.47	0.47	0.53
ASI	**0.67**	**0.03**	0.65	0.62	**0.85**	**0.03**	0.89	0.89	0.84
P (GPa)	**2.0-1.0***		1.45	1.75			0.40	0.4	0.4
T (°C)	**1250-1150***		1180	1200			1080	1050	1050
H_2O(in)			4.8	3.9			4.50	3.01	4.35
H_2O(gl)			4.95	5.2			8.30	5.9	6.3

Sample no.	LMB n=14	st.d	BM49	BM17	BM41	BA n=74	st.d	RSV49_10	BM39
SiO_2	**50.72**	**1.06**	49.61	50.72	50.65	**54.45**	**1.37**	52.43	54.31
Al_2O_3	**17.89**	**1.01**	18.18	18.27	19.22	**18.68**	**1.14**	18.85	20.20
FeO	**9.03**	**0.72**	8.32	8.12	8.27	**8.14**	**0.49**	8.03	7.50
CaO	**10.13**	**0.51**	9.81	10.41	9.42	**9.01**	**0.63**	8.37	7.53
MgO	**7.70**	**1.42**	9.04	8.94	7.27	**4.54**	**1.27**	5.48	5.19
MnO	**0.17**	**0.01**	0.15	0.15	0.17	**0.17**	**0.02**	0.19	0.12
Na_2O	**2.90**	**0.25**	3.51	2.12	3.39	**3.39**	**0.38**	3.86	3.71
K_2O	**0.39**	**0.08**	0.25	0.19	0.27	**0.53**	**0.09**	0.66	0.32
TiO_2	**0.95**	**0.14**	0.98	0.91	1.19	**0.93**	**0.09**	1.74	0.81
P_2O_5	**0.12**	**0.03**	0.12	0.12	0.15	**0.14**	**0.02**	0.40	0.19
mg#	**0.60**	**0.05**	0.66	0.66	0.61	**0.50**	**0.06**	0.55	0.55
ASI	**0.76**	**0.04**	0.76	0.81	0.84	**0.83**	**0.04**	0.85	1.00
P (GPa)	**<1.0***		1.30	1.00	1.00	**<1.0***		1.00	0.70
T (°C)	**1200-1100***		1150	1080	1065	**1050-1000***		1130	1050
H_2O(in)			4.5	4.50	2.30			0.6	2.3
H_2O(gl)			6	6.70	5.00			3.2	5.8

Sample no.	Andesite n=9	st.d	RSV49_8	RSV49_9
SiO_2	**58.95**	**1.70**	61.50	57.67
Al_2O_3	**17.78**	**0.45**	17.34	17.15
FeO	**7.11**	**0.89**	5.18	6.52
CaO	**6.86**	**0.68**	6.30	7.77
MgO	**3.43**	**1.16**	2.70	4.26

MnO	**0.17**	**0.02**	0.11	0.13
Na$_2$O	**4.03**	**0.40**	4.28	3.78
K$_2$O	**0.71**	**0.15**	0.98	0.80
TiO$_2$	**0.80**	**0.15**	1.22	1.52
P$_2$O$_5$	**0.17**	**0.04**	0.34	0.38
mg#	**0.46**	**0.1**	0.48	0.54
ASI	**0.90**	**0.06**	0.89	0.81
P (GPa)	**<1.0***		1.00	1.00
T (°C)	**950***		1030	1080
H$_2$O(in)			0.60	0.6
H$_2$O(gl)			10	7.5

(a) Map showing the Lesser Antilles volcanic arc from Puerto Rico to Trinidad & Tobago, including labelled islands: Sombrero, Saba, St. Kitts, Barbuda, Antigua, Montserrat, La Desirade, Guadeloupe, Marie Galante, Dominica, Martinique, St. Lucia, St. Vincent, Barbados, Kick'em Jenny, Grenada, Trinidad & Tobago, and Venezuela. Red triangles denote the location of active or potentially active volcanoes.

(b) Geological map of St. Vincent showing La Soufrière Volcano, Morne Garu Volcanic Centre, Grand Bonhomme Volcanic Centre, and South-East Volcanics, with RSV49 marked.

Legend:
- Alluvial & reworked deposits
- Yellow Tephra underlain by volcaniclastics
- Red scoria deposits of spatter cones
- Pyroclastic deposits of pre-Soufrière volcanic centres
- Pyroclastics deposits of Soufrière volcanic centres
- Undifferentiated volcaniclastics and lavas of Grand Bonhomme V.C.
- Lava flows, domes and associated deposits
- Eruptive centre
- Major scarp features - possible collapse scars
- inferred linear features

(a) BSE2 — 3 mm

Pd sensor capsule
Pt outer capsule
Ni + Ni(OH)$_2$
Basalt
AuPd inner capsule

(b) BSE2 — 100 μm

hbl
opx
sp
cpx
melt

(c) BSE2 — 1 mm

(d) BSE2 — 50 μm

spinel
melt
cpx
ol

2.3 wt% H₂O

Pressure (GPa) vs Temperature (°C)

hbl-pyroxenite, websterite, hbl-in, opx-in, ol-out, cpx-in, L

An₆₀, An₆₂, An₈₁

Fo₈₉, Fo₈₉, Fo₉₁, Fo₉₀, Fo₉₀, Fo₈₈, Fo₉₃

pl-in, wehrlite, hbl-gabbro, hbl-in, dunite, sp+ol-in

4.5 wt% H₂O

websterite, ol-websterite, hbl-pyroxenite, ol-out, opx-in, Fo₉₃, cpx-in, ol-in

Fo₈₇, Fo₉₃, Fo₈₉, ol-out, hbl-in, wehrlite, Fo₉₂, L+spinel

ol-px-hornblendite, Fo₉₄, Fo₉₂, opx-in, hbl-in, cpx-in

Fo₈₃, Fo₈₆, Fo₈₇, Fo₉₁, dunite

0.6 wt% H₂O

Pressure (GPa) vs Temperature (°C)

gabbronorite, websterite, dunite, cpx-in, ol-out, opx-in, pl-in

An₄₉, An₄₇, An₅₆, An₅₈, Fo₉₃, Fo₉₁

harzburgite, sp+ol-in, L

Legend hexagon: sp, ol, cpx, pl, opx, hbl

2.3 wt% H$_2$O

4.5 wt% H$_2$O

0.7 GPa

1.0 GPa

1.3 GPa

0.6 wt% H$_2$O

1.0 GPa

(a) SiO$_2$ (wt%) — *amph*

(b) Na$_2$O (wt%)

(c) K$_2$O (wt%) — *F*

(d) MgO (wt%)

(e) Cr$_2$O$_3$ (wt%)

(f) FeO$_{tot}$ (wt%) — *magnetite*

Temperature (°C)

(g) Al$_2$O$_3$ (wt%)

pl

(h) C-series

M-series

CaO (wt%)

Temperature (°C)

(k)

F

magnetite

TiO$_2$ (wt%)

Temperature (°C)

▢ 0.6 wt%	⬤ P&M, 07
▢ 2.3 wt%	⬤ P et al 02, 4.5wt% H$_2$O
▢ 4.5 wt%	○ P et al 02, 1.5wt% H$_2$O

Panel (e): Na₂O (wt%) vs MgO (wt%). Labels: *amph*, *vapor saturated*.

Panel (f): K₂O (wt%) vs MgO (wt%). Label: *F*.

Panel (g): CaO (wt%) vs MgO (wt%). Labels: *pressure*, *C-series*, *M-series*.

Legend:
- 0.6 wt% (yellow square)
- 2.3 wt% (blue square)
- 4.5 wt% (red square)
- RSV49 (green star)
- STV301 (purple star)
- P&M_07, P.et al_02 (open circle)
- St Vincent lava (grey circle)
- St Vincent MI (grey diamond)

(a) Plot of Ca p.f.u versus Mg# cpx. (b) Plot of Al_{IV} p.f.u versus Mg# opx. (c) Plot of Ti p.f.u versus Mg# opx. (d) Plot of Al_{IV} p.f.u versus Mg# amph.

Legend:
- 0.6 wt%
- 2.3 wt%
- 4.5 wt%
- lava
- P&M, 07
- P et al, 02
- cumulates

EXPERIMENTAL AND ANALYTICAL METHODS

XANES analyses

Fluorescence X-rays were normalised to the incident beam flux and collected using a 9-element solid-state detector. X-ray energy was calibrated by defining the first peak of the first derivative of Fe foil to be at 7112 eV. Spectra were recorded from 7028 eV to 7400 eV using a 0.086 eV step over the pre-edge region (7098-7123 eV), 0.259 eV step across the edge (7123-7158 eV) and 5 eV step to define the baseline (7028-7098 eV) and the post-edge region (7158-7400 eV). Counting times were 2000 ms on all points. The resulting spectra were normalised by fitting a straight line to the low-energy baseline and the post-edge region. The pre-edge feature in Fe spectra typically shows two overlapping peaks whose centroid (area-weighted) energy is sensitive to redox state (e.g Wilke et al., 2001; Berry et al., 2003; Farges et al., 2006; Cottrell et al., 2009). The pre-edge regions of the normalised spectra were fitted between 7106 and 7118 eV, using a cubic baseline combined with a Gaussian to define the rising background towards the main K-edge, and two additional Gaussian peaks to define the pre-edge region (following Berry et al., 2003; Cottrell et al., 2009). Centroid energy was related to $Fe^{3+}/\Sigma Fe$ using an empirical calibration based on synthetic basaltic standards produced under known redox conditions and analysed by Mossbauer spectroscopy ($Fe^{3+}/\Sigma Fe = 0.088$ to 0.76). Nine standards, consisting of glass chips and powder pellets of two natural basalts equilibrated at a range of fO_2 (Cottrell et al., 2009), provided by Smithsonian Institution. Direct measurement of $Fe^{3+}/\Sigma Fe$ in quenched glasses provides us with an additional monitor of experimental fO_2 via the empirical relationship of Kress & Carmichael (1991).

Appendix 1. Electron microprobe analyses of run products. FeO* is iron total. Units in parentheses are standard deviation from average analyses. Accordingly 8.88 (27) should be read as 8.88 ± 0.27. BM37* has zoned cpx.

Run No	Phase	Analyses	SiO$_2$	TiO$_2$	Al$_2$O$_3$	Cr$_2$O$_3$	FeO*	MnO	MgO	CaO	Na$_2$O	K$_2$O	P$_2$O$_5$	NiO	Total	
RSV49_2	melt	17	46.78 (42)	0.71 (02)	14.28 (20)	0.11 (02)	8.88 (27)	0.18 (06)	14.15 (16)	10.78 (09)	1.79 (09)	0.12 (02)	0.09 (03)	0.07 (04)	97.94	Mg# 74
RSV49_4	melt	19	47.55 (31)	0.80 (03)	15.21 (22)	0.12 (02)	7.84 (21)	0.21 (05)	12.40 (02)	11.51 (16)	1.85 (10)	0.15 (16)	0.08 (02)	<0.01	97.75	Mg# 74
	ol	18	41.14 (48)	<0.01	0.12 (02)	0.08 (01)	9.22 (26)	0.17 (03)	50.53 (41)	0.28 (02)	<0.01	0	0	0.22 (08)	101.79	Fo# 91
	spinel	1	0.46	0.21	43.55	21.23	12.94	0.09	19.56	0.07	0	0.01	0	0.13	98.26	Cr# 25
RSV49_11	melt	20	46.98 (36)	0.78 (03)	15.32 (22)	0.07 (05)	8.93 (35)	0.17 (04)	11.52 (28)	11.74 (22)	1.87 (10)	0.15 (02)	0.12 (03)	na	97.7	Mg# 70
	ol	5	41.70 (54)	0	0.12 (02)	0.04 (01)	7.25 (33)	0.14 (03)	51.01 (49)	0.26 (01)	<0.01	0.01	0.06 (01)	na	101.01	Fo# 93
	opx	2	51.38 (17)	0.17 (01)	7.07 (22)	0.26 (05)	6.92 (24)	0.21 (02)	30.40 (52)	2.54 (42)	0.09 (01)	0	0.03 (01)	na	99.15	En84Wo5
	spinel	2	0.50 (19)	0.22 (02)	49.59 (49)	4.77 (83)	22.62 (11)	0.09 (03)	21.15 (36)	0.11 (10)	0	0	0.02	na	99.6	Cr# 6
RSV49_6	melt	2	50.88 (67)	1.30 (10)	17.15 (18)	0.01	8.34 (37)	0.12 (03)	5.75 (19)	9.12 (20)	2.86 (52)	0.35 (03)	0.22 (01)	0	96.09	Mg# 55
	cpx	5	48.25 (59)	0.50 (15)	7.35 (34)	0.27 (04)	8.25 (29)	0.22 (06)	15.19 (68)	18.11 (64)	0.90 (10)	0.01	0.03 (02)	0.04 (03)	99.11	En46Wo40
	opx	4	53.31 (64)	0.19 (02)	6.15 (78)	0.21 (01)	8.06 (48)	0.34 (05)	31.02 (42)	2.09 (24)	0.14 (04)	<0.01	0.02 (01)	0.10 (03)	101.64	En83Wo4
	pl	5	52.90 (73)	0.07 (01)	28.41 (47)	<0.01	1.70 (46)	<0.01	0.29 (15)	11.85 (53)	4.65 (23)	0.11 (02)	<0.01	0	100.04	An# 58
	spinel	1	0.22	0.51	43.62	0.05	33.54	0.14	18.81	0.19	0	0	0.02	0.49	97.61	Cr# 0
RSV49_10	melt	3	49.41 (34)	1.64	17.76 (03)	0	7.57 (26)	0.18 (03)	5.16 (19)	7.88 (21)	3.63 (20)	0.62 (03)	0.37 (01)	<0.01	94.23	Mg# 55
	cpx	4	47.99 (76)	0.76 (08)	7.33 (72)	0.16 (04)	8.15 (31)	0.25 (02)	14.68 (49)	19.17 (13)	0.94 (04)	0	0.03	0.07 (05)	99.51	En44Wo42
	opx	3	51.34 (81)	0.32 (02)	7.49 (65)	0.11 (05)	10.35 (16)	0.26 (02)	29.52 (34)	1.44 (14)	0.13 (03)	<0.01	<0.01	0.15 (04)	101.15	En81Wo3
	pl	1	54.04	0.06	29.07	0.013	1.15	0.05	0.16	11.8	5.10	0.14	0.04	0	101.63	An# 56
	spinel	2	0.23 (08)	0.66 (05)	43.59 (01)	0.11 (07)	36.25 (90)	0.17 (06)	16.55 (10)	0.18 (02)	0	0	0.02	0.58 (03)	98.36	Cr# 0.1
RSV49_9	melt	6	53.97 (62)	1.42 (02)	16.05 (21)	0.02 (01)	6.10 (09)	0.12 (04)	3.98 (21)	7.27 (35)	3.54 (14)	0.75 (04)	0.36 (06)	<0.01	93.58	Mg# 54
	cpx	6	49.80 (90)	0.57 (09)	6.23 (58)	0.19 (03)	8.24 (34)	0.22 (04)	14.56 (38)	19.43 (44)	1.16 (13)	0.02	0.04 (01)	0.07 (02)	100.5	En44Wo42
	opx	4	53.43 (70)	0.22 (02)	5.74 (62)	0.09 (03)	9.60 (46)	0.28 (03)	30.74 (43)	1.26 (10)	0.08 (03)	<0.01	<0.01	0.12 (03)	101.59	En83Wo2
	pl	3	57.70 (62)	0.04 (02)	26.50 (98)	0	1.09 (16)	0	0.11 (01)	9.48 (53)	5.87 (01)	0.19	<0.01	<0.01	101.02	An# 47
	spinel	4	0.19 (11)	0.47 (01)	45.82 (65)	0.24 (06)	31.86 (84)	0.17 (02)	17.32 (33)	0.15 (05)	0	0	0	0.58 (05)	96.83	Cr# 0.3
RSV49_8	melt	7	55.86 (48)	1.11 (04)	15.75 (25)	<0.01	4.70 (16)	0.10 (04)	2.45 (27)	5.72 (09)	3.89 (11)	0.89 (03)	0.31 (06)	<0.01	90.82	Mg# 48
	cpx	1	50.75	0.59	5.16	0.13	7.61	0.29	14.75	19.63	0.98	<0.01	0.02	0.04	99.97	En44Wo42
	opx	2	55.03 (72)	0.25 (05)	4.69 (59)	0.14 (08)	12.92 (49)	0.28	28.11 (10)	1.41 (26)	0.11 (01)	0.04 (03)	0.05	0.13 (07)	103.15	En77Wo3
	pl	3	55.15 (24)	0.04	26.89 (25)	0	0.69 (02)	0	0.06 (02)	9.87 (38)	5.58 (27)	0.13 (01)	<0.1	<0.1	98.44	An# 49
	spinel	2	0.28 (21)	0.38 (04)	56.63 (47)	0.06 (05)	26.72 (05)	0.16	16.36 (10)	0.19 (04)	0	0	0	0.34 (01)	101.14	Cr# 0
	ilminite	1	0	22.35	2.44	0.36	59.02	0.07	4.71	0.45	0	0	0	0.14	89.57	
bmn1	melt	21	46.55 (3)	0.86 (02)	16.61 (1)	0.03 (01)	7.09 (2)	0.16 (04)	7.08 (15)	12.14 (2)	2.46 (2)	0.18 (03)	0.1 (02)	< 0.01	93.28	Mg# 64
	ol	12	40.88 (2)			0.07 (02)	0.04 (01)	9.86 (9)	0.17 (03)	48.0 (8)	0.22 (02)			0.35 (09)	99.59	Fo# 90
	cpx	12	48.54 (6)	0.55 (06)	6.32 (5)	0.19 (06)	6.66 (04)	0.11 (02)	14.17 (27)	22.28 (33)	0.32 (03)		0.03 (02)	0.03 (01)	99.21	En42Wo47
	spinel		0.22	0.73	26.46	32.41	25.7	0.28	14.57	0.22					100.59	Cr# 45
	spinel*		0.37	1.7	34.05	18.28	28.83	0.22	15.91	0.16					99.52	Cr# 26
BM38	melt	24	46.44 (3)	0.79 (02)	14.99 (27)	0.05 (006)	8.49 (18)	0.17 (04)	11.34 (5)	11.29 (15)	2.15 (13)	0.15 (03)	0.08 (02)	< 0.01	95.95	Mg# 70
	ol	17	40.69 (4)	0.02 (01)	0.17 (1)	0.06 (08)	7.31 (16)	0.15 (02)	50.86 (4)	0.33 (11)				0.38 (02)	99.99	Fo# 93
	spinel	1	0	0.49	29.9	16.79	29.87	0.12	19.31	0.56	0.02			0.52	97.6	Cr# 27
BM40	melt	21	46.88 (4)	0.89 (02)	17.01 (13)	0.02 (01)	8.27 (17)	0.15 (03)	8.30 (12)	11.33 (09)	2.37 (16)	0.17 (02)	0.11 (03)	< 0.01	95.52	Mg# 64
	ol	17	39.80 (37)	0.02 (01)	0.17 (1)	0.02 (006)	10.04 (15)	0.18 (017)	48.82 (28)	0.33 (1)				0.30 (02)	99.69	Fo# 90
	cpx	16	47.86 (8)	0.47 (08)	6.92 (9)	0.51 (1)	6.16 (37)	0.11 (6)	15.42 (6)	20.69 (5)	0.38 (04)		0.03 (01)	0.05 (02)	98.6	En45Wo44
	spinel	1	1.62	0.52	31.12	15.03	31.82	0.18	16.61	0.53	0.14			0.37	97.95	Cr# 25
BM43	melt	24	46.52 (45)	0.85 (08)	17.14 (3)	0.02 (01)	8.28 (47)	0.17 (03)	7.76 (54)	10.91 (62)	2.39 (13)	0.18 (03)	0.11 (03)	< 0.01	94.33	Mg# 63

Sample	Phase	n	SiO₂	TiO₂	Al₂O₃	Cr₂O₃	FeO	MnO	MgO	CaO	Na₂O	K₂O	P₂O₅	NiO	Total	
	ol	9	40.45 (23)	0.02 (01)	0.13 (19)	0.01 (005)	9.16 (14)	0.2 (02)	49.11 (26)	0.3 (05)				0.37 (02)	99.75	Fo# 91
	cpx	3	48.38 (46)	0.42 (04)	6.81 (63)	0.52 (04)	6.04 (18)	0.13 (015)	15.37 (36)	21.06 (17)	0.39 (05)			0.05 (01)	99.17	En45Wo44
	spinel	10	0.32 (23)	0.57 (01)	27.58 (89)	8.9 (88)	42.31 (4)	0.19 (01)	14.96 (13)	0.26 (06)				0.56 (02)	95.6	Cr# 18
BM39	melt	2	50.73 (30)	0.76 (02)	18.86 (22)	0.07	7.00 (38)	0.11 (00)	4.85 (33)	7.04 (01)	3.46 (06)	0.30 (01)	0.18 (02)	0.05 (04)	93.4	Mg# 55
	cpx	2	48.03 (19)	0.66 (08)	9.15 (47)	0.08 (007)	7.12 (14)	0.15 (01)	14.23 (58)	19.94 (33)	0.91 (01)	0.037 (01)	0.04 (02)	0.07 (02)	100.4	En43Wo44
	opx	9	52.16 (55)	0.23 (03)	7.33 (66)	0.07 (04)	7.41 (68)	0.22 (02)	31.18 (78)	1.52 (4)				0.09 (03)	100.2	En85Wo3
	hbl	9	41.57 (63)	1.53 (11)	14.71 (52)	0.11 (02)	8.53 (46)	0.11 (02)	16.29 (24)	11.57 (53)	2.76 (11)	0.14 (02)	0.03 (02)	0.10 (03)	97.34	Mg# 77
	spinel	5	0.51 (15)	0.71 (02)	21.43 (22)	0.98 (07)	53.91 (38)	0.35 (02)	16.18 (13)	0.35 (07)				1.10 (09)	95.57	Cr# 3
BM58	melt	1	66.08	0.07	13.08	0	1.26	0.02	1.19	2.68	2.49	0.99	0.12	0.027	88.03	Mg# 63
	cpx	2	52.26 (86)	0.41 (32)	2.56 (1.16)	0	6.86 (1.12)	0.24 (04)	16.40 (1.99)	19.68 (50)	0.94 (29)	0.01	0.02	0.10 (01)	99.78	En50Wo40
	opx	1	53.47	0.2	7.53	0.08	8.49	0.28	27.62	2.46	0.31	0.037	0.036	0.05	100.57	En80Wo5
	hbl	3	41.60 (27)	1.2 (08)	14.72 (32)	0.14 (01)	8.63 (16)	0.11 (02)	16.11 (22)	11.42 (18)	2.40 (07)	0.13 (03)	0.03 (02)	0.09 (01)	96.59	Mg# 77
	pl	1	47.19	0.01	32.42	0.01	1.48	0.01	0.08	16.38	2.10	0.04	0.01	0.00	99.74	An# 80
	spinel	5	0.26 (01)	4.56 (99)	1.47 (24)	0.52 (41)	80.53 (64)	0.04 (02)	0.66 (19)	0.26 (03)				0.04 (02)	88.34	Cr# 19
BM3	melt	18	47.53 (39)	0.81 (03)	16.02 (34)	0.07 (01)	7.72 (15)	0.16 (03)	9.16 (07)	11.64 (35)	2.11 (2)	0.16 (02)	0.1 (02)	0.10 (06)	95.58	Mg# 68
	ol	9	41.07 (50)	0.03 (02)	0.46 (45)	0.071 (03)	10.54 (13)	0.18 (02)	46.97 (70)	0.49 (23)				0.82 (19)	100.63	Fo# 89
	cpx	1	51.45	0.2	5.59	1.35	4.44	0.16	17.73	18.36	0.47		0.03	0.31	100.09	En53Wo39
	spinel	na														
BM6	melt	20	46.88 (29)	0.86 (04)	16.13 (22)	0.06 (014)	6.63 (16)	0.16 (02)	9.41 (15)	10.96 (09)	2.15 (11)	0.15 (01)	0.12 (03)	< 0.01	93.52	Mg# 72
	ol	3	40.67 (44)	0.01 (01)	0.06 (02)	0.06 (014)	11 (7)	0.13 (03)	48.45 (47)	0.23 (02)				0.21 (02)	100.82	Fo# 89
	cpx	4	49.91 (36)	0.37 (05)	6.81 (36)	0.82 (19)	4.66 (25)	0.11 (01)	16.26 (25)	19.68 (24)	0.44 (09)	0.01 (002)	0.04 (02)	0.03 (03)	99.14	En49Wo43
	spinel		0.5	0.31	35.74	28.68	13.58	0.23	17.35	0.22					96.62	Cr# 35
BM16	melt	25	45.59 (35)	1.03 (05)	16.64 (13)	0.01 (01)	8.82 (17)	0.18 (03)	8.41 (26)	9.68 (08)	2.95 (20)	0.23 (02)	0.14 (03)	0.5 (02)	94.18	Mg# 63
	cpx	5	48.27 (48)	0.41 (06)	7.38 (44)	0.15 (08)	7.06 (32)	0.16 (01)	15.99 (7)	19.01 (43)	0.69 (03)			0.13 (03)	99.25	En49Wo43
	opx	7	51.49 (54)	0.18 (02)	7.12 (46)	0.09 (03)	8.26 (66)	0.17 (01)	30.55 (72)	1.68 (2)	0.07 (03)	< 0.01		0.23 (07)	99.84	En84Wo3
	spinel	3	0.34 (16)	0.53 (06)	36.86 (8)	3.01 (33)	38.07 (78)	0.19 (03)	15.90 (39)	0.20 (01)				1.62 (14)	96.72	Cr# 5
BM41	melt	16	47.25 (33)	1.11 (02)	17.93 (19)	0	7.71 (24)	0.16 (04)	6.78 (58)	8.79 (11)	3.16 (18)	0.25 (02)	0.14 (02)	< 0.01	93.28	Mg# 61
	cpx	17	48.12 (29)	0.50 (05)	7.54 (65)	0.13 (05)	6.84 (22)	0.14 (03)	15.41 (36)	19.58 (34)	0.66 (09)	< 0.01	0.03 (02)	0.05 (01)	99.00	En46Wo42
	opx	14	51.64 (62)	0.18 (02)	6.95 (60)	0.09 (04)	8.16 (46)	0.18 (02)	30.95 (55)	1.56 (20)	0.08 (04)	< 0.01	< 0.01	0.09 (02)	99.92	En84Wo3
	spinel	9	0.44 (27)	0.42 (02)	46.06 (67)	1.74 (41)	29.88 (47)	0.15 (02)	17.93 (34)	0.18 (04)				0.49 (03)	97.28	Cr# 3
BM13	melt	6	47.37 (70)	0.83 (03)	18.83 (30)	0.04 (01)	8.10 (37)	0.15 (03)	6.33 (68)	8.92 (29)	2.69 (14)	0.24 (03)	0.20 (04)	0	93.7	Mg# 58
	cpx	8	49.25 (77)	0.49 (06)	7.39 (93)	0.15 (05)	7.13 (76)	0.19 (06)	14.16 (43)	20.17 (83)	0.72 (14)		0.03 (02)	0.05 (04)	99.76	En43Wo44
	opx	2	52.92 (33)	0.17 (08)	5.65 (94)	0.05 (02)	10.64 (15)	0.23 (04)	28.95 (89)	1.53 (21)	0.09 (02)			0.05 (0)	100.29	En80Wo3
	hbl	35	41.73 (68)	1.27 (11)	15.60 (51)	0.18 (04)	8.78 (31)	0.12 (02)	15.53 (54)	10.82 (27)	2.71 (1)	0.17 (01)		0.09 (03)	97.04	Mg# 76
	spinel		0.41	0.23	59.5	0.69	21.5	0.12	17.34	0.19					99.98	Cr# 0.8
BM52	melt	2	56.72 (2)	0.24 (02)	15.11 (26)	0.03 (0)	3.42 (17)	0.12 (03)	3.72 (16)	8.41 (35)	2.45 (004)	0.32 (0)	0.29 (03)	0.02 (005)	90.85	Mg# 66
	cpx	5	50.11 (9)	0.44 (2)	7.14 (6)	0.13 (06)	7.38 (45)	0.20 (02)	13.85 (3)	19.58 (8)	0.75 (08)			0.04 (01)	99.74	En43Wo44
	opx	5	53.76 (17)	0.14 (03)	3.95 (6)		10.62 (06)	0.26 (02)	28.67 (39)	1.64 (2)	0.09 (05)	< 0.01	0.013 (006)	0.10 (008)	99.48	En79Wo3
	hbl	16	42.13 (4)	1.10 (11)	15.39 (35)	0.19 (04)	9.38 (32)	0.21 (17)	15.02 (3)	11.13 (25)	2.31 (10)	0.14 (009)		0.10 (01)	97.27	Mg# 74
	spinel	3	0.34 (3)	7.34 (6)	2.99 (05)	0.37 (12)	76.61 (43)	0.10 (02)	1.83 (16)	0.38 (05)				0.10 (01)	90.07	Cr# 8
BM15	melt	3	59.00 (1)	0.22 (05)	16.74 (22)	0	2.57 (07)	0.10 (02)	2.26 (22)	5.91 (21)	2.86 (13)	0.41 (01)	0.28 (02)	< 0.01	90.71	Mg# 65
	cpx	na														
	opx	4	49.8 (2)	0.13 (05)	10.13 (4)	0.1	8.86 (5)	0.21 (01)	29.47 (36)	1.31 (15)	0.15 (03)			0.08 (01)	100.24	En83Wo3
	hbl	7	41.73 (77)	1.11 (24)	15.16 (36)	0.11 (02)	8.90 (35)	0.15 (03)	16.09 (24)	10.68 (41)	2.38 (14)	0.13 (01)	0.04 (02)	0.13 (03)	96.75	Mg# 76
	spinel	6	1.14 (66)	10.23 (54)	3.66 (17)	0.29 (18)	73.24 (78)	0.08 (01)	1.98 (16)	0.35 (05)				0.11 (02)	91.12	Cr# 5
	pl	3	52.40 (67)	< 0.01	28.99 (9)	0.03 (01)	1.12 (09)	< 0.01	0.45 (4)	12.28 (2)	4.56 (14)	0.04	0.04		99.98	An# 60

		n													Total	
BM60	melt	na														
	cpx	3	48.84 (2)	0.31 (03)	7.29 (67)	0.20 (01)	7.02 (27)	0.16 (03)	15.29 (4)	19.37 (67)	0.70 (01)			0.03 (0)	0.06 (02)	99.28 En46Wo42
	opx	5	52.63 (6)	0.13 (02)	7.17 (59)	0.18 (04)	6.90 (37)	0.17 (04)	30.71 (6)	1.72 (14)	0.13 (03)			0.12 (03)	99.86 En86Wo3
	hbl	20	43.55 (54)	0.89 (01)	13.34 (69)	0.09 (07)	9.49 (37)	0.17 (02)	15.34 (36)	11.60 (46)	2.00 (07)	0.11 (02)	0.05 (02)	0.08 (02)	96.72 Mg# 74
	spinel	3	0.19 (01)	0.23 (02)	46.36 (8)	0.75 (01)	31.23 (74)	0.23 (01)	17.66 (19)	0.15 (03)				0.75 (01)	97.01 Cr# 1
	pl	2	51.86 (8)	0.14 (02)	27.54 (76)		1.73 (33)	0.05 (03)	1.43 (26)	12.42 (8)	4.11 (33)	0.07 (0)	0.04 (01)	0.05 (02)	99.42 An# 62
BM45	melt	30	45.81 (3)	0.71 (02)	13.92 (14)	0.13 (01)	8.58 (18)	0.16 (03)	13.98 (22)	10.57 (10)	1.98 (09)	0.14 (01)	0.09 (03)	0.05 (03)	96.1 Mg# 74
	spinel	na													
BM56	melt	na													
	cpx	8	46.78 (39)	0.66 (11)	9.73 (39)	0.08 (02)	7.65 (22)	0.14 (03)	13.02 (46)	19.74 (49)	1.04 (11)			0.03 (01)	0.05 (02)	98.93 En41Wo45
	opx	17	50.93 (34)	0.19 (03)	8.98 (7)	0.13 (06)	8.05 (31)	0.20 (03)	29.29 (63)	1.40 (46)	0.16 (06)			0.13 (03)	99.49 En84Wo3
	spinel	5	0.17 (03)	0.47 (02)	44.11 (6)	0.38 (15)	33.55 (5)	0.17 (02)	16.99 (14)	0.15 (06)				0.72 (01)	96.67 Cr# 0.6
BM30	melt	6	46.07 (7)	0.91 (11)	16.80 (9)	0.04 (01)	8.364 (3)	0.18 (02)	9.74 (9)	9.47 (9)	3.10 (7)	0.24 (07)	0.11 (02)	0.03 (01)	95.1 Mg# 67
	cpx	10	48.42 (5)	0.41 (07)	8.23 (6)	0.26 (11)	6.75 (38)	0.15 (02)	15.68 (47)	18.76 (41)	0.89 (07)	< 0.01	0.01 (01)	0.06 (02)	99.62 En47Wo40
	opx	8	51.72 (46)	0.15 (02)	7.44 (31)	0.17 (07)	8.42 (24)	0.17 (01)	30.47 (46)	1.55 (15)	0.17 (24)	< 0.01	< 0.01	0.12 (02)	100.39 En84Wo3
	spinel	4	0.22 (05)	0.28 (02)	50.84 (7)	2.01 (3)	25.63 (29)	0.14 (01)	19.34 (26)	0.15 (03)				0.49 (01)	99.16 Cr# 3
BM57	melt	5	47.61 (99)	1.05 (14)	17.85 (9)	< 0.01	6.35 (9)	0.21 (05)	4.09 (9)	9.45 (99)	2.40 (65)	0.21 (1)	0.18 (02)	< 0.01	89.40 Mg# 53
	cpx	11	47.77 (6)	0.64 (09)	9.13 (7)	0.17 (03)	7.38 (3)	0.16 (01)	13.76 (5)	19.07 (6)	0.98 (06)			0.02 (01)	0.06 (02)	99.13 En43Wo43
	opx	14	51.53 (8)	0.19 (03)	8.3 (8)	0.13 (04)	8.27 (5)	0.19 (02)	29.38 (7)	1.36 (24)	0.12 (05)	< 0.01	< 0.01	0.11 (01)	99.61 En84Wo3
	spinel	5	0.21 (06)	0.27 (01)	50.19 (8)	0.98 (4)	25.32 (57)	0.14 (02)	19.77 (2)	0.14 (02)				0.62 (01)	97.64 Cr# 2
bmn2	melt	9	49.43 (54)	0.99 (02)	19.95 (53)	0.01 (007)	6.49 (32)	0.14 (03)	3.23 (5)	9.78 (4)	2.63 (4)	0.22 (02)	0.12 (03)	0.03 (03)	93.02 Mg# 47
	ol	14	40.10 (28)	0.03 (02)	0.14 (13)	0.28 (01)	13.59 (27)	0.23 (03)	44.70 (4)	0.32 (1)				0.26 (09)	99.65 Fo# 85.4
	cpx	9	48.26 (6)	0.60 (06)	6.87 (5)	0.36 (09)	6.49 (39)	0.13 (02)	14.22 (24)	21.45 (3)	0.33 (02)	< 0.01	0.02 (01)	0.04 (01)	98.78 En43Wo46
	spinel		0.43	0.74	42.91	16.13	22.31	0.19	16.63	0.24					99.58 Cr# 20
BM33	melt	26	45.37 (27)	0.70 (04)	13.88 (19)	0.13 (01)	7.30 (26)	0.34 (9)	13.63 (21)	10.30 (13)	2.23 (13)	0.14 (01)	0.08 (03)	0.019 (03)	94.2 Mg# 77
	spinel	na													
BM37*	melt	33	45.93 (13)	0.82 (02)	15.85 (32)	0.01 (01)	7.58 (2)	0.15 (03)	8.35 (13)	11.73 (23)	2.67 (13)	0.16 (02)	0.09 (02)	0.02 (02)	93.36 Mg# 66
	ol	18	40.82 (4)	0.02 (02)	0.12 (17)	0.01	5.82 (24)	0.16 (02)	52.76 (56)	0.27 (1)				0.36 (03)	100.33 Fo# 94.2
	cpx	18	44.77 (8)	0.69 (17)	8.07 (47)	0.12 (05)	8.09 (35)	0.10 (02)	13.91 (4)	21.63 (17)	0.43 (03)			0.02 (01)	0.04 (02)	97.88 En41Wo46
	cpx[z]	15	49.17 (76)	0.30 (03)	4.27 (23)	0.10 (02)	5.78 (19)	0.12 (01)	17.25 (28)	20.75 (29)	0.36 (02)			0.02 (01)	0.04 (01)	98.16 En48Wo42
	spinel	3	0.31 (2)	0.79 (01)	13.27 (09)	5.66 (005)	60.21 (5)	0.25 (01)	13.10 (14)	0.31 (06)				0.58 (03)	94.49 Cr# 22
BM34	melt	16	51.23 (5)	0.42 (03)	17.64 (35)	< 0.01	4.65 (27)	0.17 (04)	4.83 (12)	7.81 (11)	2.92 (13)	0.26 (02)	0.17 (04)	< 0.01	90.01 Mg# 65
	ol	16	41.05 (44)	< 0.01	0.07 (03)	< 0.01	6.09 (24)	0.20 (02)	52.33 (47)	0.23 (06)	0.02 (01)			0.41 (04)	100.43 Fo# 94
	cpx	6	48.87 (8)	0.40 (07)	5.81 (8)	0.25 (2)	6.35 (5)	0.14 (04)	15.88 (87)	21.47 (37)	0.45 (05)	< 0.01	0.024 (01)	0.07 (03)	99.71 En45Wo44
	hbl	9	41.65 (56)	1.13 (19)	13.99 (47)		7.78 (12)	0.15 (01)	17.27 (3)	11.23 (23)	2.62 (1)	0.09 (006)	0.03 (01)	0.08 (01)	96.12 Mg# 80
	spinel	4	0.15 (01)	0.93 (16)	17.69 (32)	2.84 (33)	59.01 (28)	0.34 (02)	11.69 (35)	0.24 (06)				0.59 (06)	93.49 Cr# 10
BM36	melt	20	51.49 (52)	0.42 (03)	17.43 (21)	< 0.01	4.69 (2)	0.15 (03)	4.76 (48)	8.46 (11)	2.66 (18)	0.24 (02)	0.18 (04)	< 0.01	90.48 Mg# 64
	cpx	4	48.29 (9)	0.59 (08)	6.61 (5)	0.14 (03)	6.42 (4)	0.15 (03)	15.72 (48)	21.21 (57)	0.54 (16)			0.02 (01)	0.03 (02)	99.72 En45Wo43
	opx	15	52.69 (8)	0.17 (03)	5.79 (7)	0.07 (01)	7.28 (45)	0.25 (03)	32.60 (47)	1.38 (21)				0.07 (02)	100.34 En86Wo3
	hbl	26	42.63 (68)	0.98 (12)	13.26 (44)	0.12 (03)	8.09 (45)	0.13 (02)	18.06 (3)	11.50 (18)	2.49 (1)	0.10 (02)		0.08 (02)	97.51 Mg# 80
	spinel	4	0.24 (04)	0.66 (01)	9.12 (17)	1.77 (1)	70.67 (64)	0.37 (03)	9.78 (2)	0.33 (04)				0.63 (03)	93.59 Cr# 12
BM23	melt	8	44.30 (32)	0.66 (03)	13.84 (21)	0.09 (01)	8.28 (21)	0.15 (01)	13.66 (18)	10.29 (1)	2.05 (18)	0.13 (01)	0.08 (03)	0.07 (03)	93.6 Mg# 75

Sample	Phase	n	SiO2	TiO2	Al2O3	Cr2O3	FeO	MnO	MgO	CaO	Na2O	K2O	P2O5	NiO	Total	
	spinel		0.27	0.35	25.61	21.12	30.45	0.22	18.26	0.24					96.51	Cr# 36
BM9	melt	16	45.27 (24)	0.79 (04)	15.98 (2)	0.04 (01)	7.90 (17)	0.14 (02)	8.57 (3)	11.03 (12)	2.49 (17)	0.16 (02)	0.09 (03)	< 0.01	92.46	Mg# 66
	ol	7	40.57 (4)	0.02 (02)	0.06 (05)	0.03 (01)	10.97 (18)	0.17 (02)	47.63 (2)	0.24 (04)				0.19 (03)	99.89	Fo# 89
	cpx	5	51.74 (96)	0.33 (08)	4.18 (1.21)	0.61 (2)	4.96 (1.3)	0.11 (01)	16.27 (1.1)	20.53 (1)	0.64 (19)	0.02 (01)		< 0.01	99.39	En48Wo43
	spinel	6	0.27 (06)	0.41 (04)	34.78 (8)	23.21 (9)	22.42 (09)	0.12 (04)	16.01 (26)	0.23 (06)				0.14 (02)	97.6	Cr# 31
BM17	melt	3	45.58 (51)	0.75 (04)	14.61 (18)	0.03 (01)	8.58 (26)	0.20 (07)	10.91 (08)	10.99 (69)	2.28 (18)	0.17 (01)	0.13 (02)	0.03 (02)	94.23	Mg# 66
	ol	7	41.48 (24)	<0.01	0.27 (19)	<0.01	6.84 (35)	0.16 (02)	51.22 (5)	0.20 (07)	0.03 (02)			0.43 (01)	100.69	Fo# 93
	cpx	7	48.68 (6)	0.39 (06)	7.07 (69)	0.16 (04)	6.62 (2)	0.14 (02)	15.59 (67)	20.19 (77)	0.68 (15)	<0.01	0.02 (01)	0.05 (01)	99.62	En46Wo43
	spinel	2	0.40 (8)	0.65 (01)	25.18 (17)	2.92 (01)	49.03 (9)	0.21 (01)	15.55 (7)	0.32 (17)				0.80 (01)	95.76	Cr# 7
BM24	melt	1	45.45	0.80	17.93	0.00	8.96	0.15	7.21	9.01	2.54	0.29	0.14	0.00	92.49	Mg# 59
	ol	12	41.09 (19)	0.02 (006)	0.15 (08)	0.02 (01)	12.64 (19)	0.19 (06)	46.97 (28)	0.17 (04)				0.30 (03)	101.58	Fo# 87
	cpx	7	50.11 (5)	0.43 (06)	6.41 (49)	0.23 (06)	6.55 (29)	0.16 (03)	15.48 (29)	19.97 (27)	0.55 (07)		0.03 (01)	0.06 (01)	99.99	En46Wo43
	hbl	12	42.94 (56)	0.92 (07)	14.65 (55)	0.16 (04)	8.17 (19)	0.11 (02)	17.16 (2)	10.99 (2)	2.86 (1)	0.14 (02)	0.2 (01)	0.09 (02)	98.37	Mg# 79
	spinel	20	0.19 (09)	0.62 (21)	42 (2.7)	5.21 (1.1)	33.03 (3.8)	0.18 (02)	15.35 (85)	0.17 (03)				0.41 (03)	97.16	Cr# 8
BM46	melt	30	45.26 (28)	0.68 (02)	13.69 (18)	0.13 (01)	7.36 (14)	0.15 (02)	13.69 (17)	10.27 (11)	2.23 (12)	0.14 (01)	0.08 (02)	0.01 (01)	93.69	Mg# 77
	spinel	na														
BM49	melt	25	45.08 (28)	0.89 (02)	16.52 (17)	<0.01	7.56 (18)	0.14 (04)	8.21 (2)	8.91 (28)	3.19 (34)	0.23 (02)	0.11 (02)	0.02 (02)	90.87	Mg# 66
	ol	6	41.07 (23)	0.01 (01)	0.07 (02)	0.01 (007)	7.17 (45)	0.17 (02)	51.04 (42)	0.18 (08)				0.44 (02)	100.19	Fo# 93
	cpx	23	48.47 (68)	0.42 (06)	7.04 (65)	0.11 (02)	6.53 (32)	0.12 (05)	15.40 (66)	19.88 (64)	0.80 (07)	<0.01	0.02 (01)	0.06 (02)	98.86	En46Wo43
	opx	17	51.89 (52)	0.14 (02)	6.85 (36)	0.10 (03)	7.46 (46)	0.17 (01)	31.49 (53)	1.27 (18)	0.07 (01)	< 0.01	< 0.01	0.11 (01)	99.58	En86Wo2
	spinel	8	0.20 (04)	0.63 (03)	34.82 (72)	1.57 (38)	40.51 (61)	0.17 (01)	16.00 (17)	0.18 (03)				0.75 (02)	94.83	Cr# 3
BM32	melt	5	46.48 (82)	0.89 (10)	17.83 (09)	< 0.01	6.75 (92)	0.15 (04)	7.88 (62)	8.61 (52)	3.12 (27)	0.28 (04)	0.17 (01)	0.02 (01)	92.18	Mg# 68
	cpx	5	48.86 (31)	0.41 (09)	7.03 (57)	0.15 (07)	6.39 (35)	0.13 (01)	15.91 (41)	19.87 (58)	0.78 (07)	< 0.01	0.03 (01)	0.08 (02)	99.64	En47Wo42
	opx	5	52.22 (5)	0.17 (02)	7.13 (02)	0.13 (02)	7.77 (09)	0.17 (02)	31.11 (43)	1.5 (44)	< 0.01	0.01 (01)	< 0.01	0.13 (01)	100.72	En85Wo3
	spinel	2	0.9 (05)	0.50 (03)	38.71 (42)	2.65 (004)	35.29 (59)	0.15 (02)	18.02 (56)	0.29				0.81 (03)	97.42	Cr# 4
BM50	melt	4	49.36 (6)	0.56 (06)	18.27 (36)	0.02 (01)	4.45 (25)	0.14 (03)	1.95 (26)	8.56 (39)	1.77 (1)	0.24 (02)	0.25 (07)	< 0.01	85.57	Mg# 44
	cpx	9	48.69 (65)	0.43 (06)	7.51 (97)	0.12 (03)	7.94 (6)	0.19 (04)	14.00 (84)	19.40 (76)	1.04 (27)	< 0.01	0.03 (01)	0.04 (01)	99.41	En43Wo43
	opx	6	51.49 (71)	0.15 (01)	7.92 (72)	0.12 (02)	9.41 (52)	0.23 (02)	29.02 (70)	1.57(47)				0.09 (02)	100.15	En81Wo4
	hbl	14	41.86 (33)	0.88 (07)	14.91 (42)	0.16 (02)	8.81 (18)	0.12 (02)	16.27 (46)	10.91 (18)	2.76 (13)	0.16 (01)		0.09 (02)	97.06	Mg# 77
	spinel	5	0.21 (04)	1.00 (02)	20.26 (24)	1.89 (21)	60.56 (38)	0.25 (02)	9.37 (06)	0.27 (02)				0.56 (03)	94.4	Cr# 6